



**HAL**  
open science

## Experimental study of sediment transport processes by liquid water and brine under Martian pressure

Meven Philippe, S.J. Conway, J. Raack, S. Carpy, M. Massé, M.R. Patel, M.E. Sylvest, S.R. Lewis, C. Morino

► **To cite this version:**

Meven Philippe, S.J. Conway, J. Raack, S. Carpy, M. Massé, et al.. Experimental study of sediment transport processes by liquid water and brine under Martian pressure. *Icarus*, 2023, 395, pp.115475. 10.1016/j.icarus.2023.115475 . hal-04005921

**HAL Id: hal-04005921**

**<https://hal.science/hal-04005921>**

Submitted on 27 Feb 2023

**HAL** is a multi-disciplinary open access archive for the deposit and dissemination of scientific research documents, whether they are published or not. The documents may come from teaching and research institutions in France or abroad, or from public or private research centers.

L'archive ouverte pluridisciplinaire **HAL**, est destinée au dépôt et à la diffusion de documents scientifiques de niveau recherche, publiés ou non, émanant des établissements d'enseignement et de recherche français ou étrangers, des laboratoires publics ou privés.



Distributed under a Creative Commons Attribution 4.0 International License

## Experimental study of sediment transport processes by liquid water and brine under Martian pressure

M. Philippe<sup>1\*</sup>, S. J. Conway<sup>1</sup>, J. Raack<sup>2,3</sup>, S. Carpy<sup>1</sup>, M. Massé<sup>1</sup>, M. R. Patel<sup>4</sup>, M. E. Sylvest<sup>4</sup>, S. R. Lewis<sup>4</sup>, C. Morino<sup>5</sup>

<sup>1</sup>Laboratoire de Planétologie et Géosciences, CNRS UMR 6112, Nantes Université/Université d'Angers/Le Mans Université, 2 chemin de la Houssinière, Nantes France.

<sup>2</sup>Innomago GmbH, Ludgerstraße 110, 48143 Münster, Germany.

<sup>3</sup>Institut für Planetologie, Westfälische Wilhelms-Universität Münster, Wilhelm-Klemm-Str. 10, 48149 Münster, Germany.

<sup>4</sup>School of Physical Sciences, Open University, Milton Keynes, UK.

<sup>5</sup>Laboratoire EDYTEM, Université Savoie Mont Blanc, CNRS UMR 5204, 5 Bd de la Mer Caspienne, 73370 Le Bourget-du-Lac, France.

### Highlights:

- Water and brine releases boil under current Martian pressure
- Above 10 °C, boiling ejects large volumes of sediment
- Water and MgSO<sub>4</sub> brine transport similar volumes of sediment...
- ...but brine produces more pellets, and thus should form longer morphologies on Mars
- Our experimental conditions can be met on Mars under certain conditions

**Keywords:** Mars, surface; Mars, climate; Experimental techniques; Geological processes

**Abstract:** We present here an experimental study to compare the behaviour of water and brine releases over loose sediments under present-day Martian pressure. Water has been invoked to explain current or past Martian surface features for decades. Recent studies have indicated that current surface conditions are, in certain times and places, compatible with the transient existence of liquid water or brine. However, the behaviour of water or brine releases over loose sediments under low Martian atmospheric pressure has been poorly studied.

We performed 33 experiments of water and brine (MgSO<sub>4</sub> at 19 wt%) releases over sandy slopes of various temperatures (0 °C to 20 °C), in a chamber allowing the reproduction of Martian pressure – 6 – 7 millibars (mbar). We observe sediment transport mechanisms, that do not occur on Earth, caused by the boiling of water or brine at Martian pressures: grain ejection and “levitation” of sand pellets on cushions of vapour. The main parameter controlling the behaviour of the flow is the temperature of the substrate. Water and brine flows transport similar volumes of sediment under Martian pressure. We show that the grain ejection is the most efficient transport mechanism, dominating the volumes of sediment transported. Pellet “levitation” should lead to longer features formed with brine than with pure water on Mars. Boiling induced sediment transport requires much less water than sediment transport by overland flow to form morphologies similar in size or volume. Moreover, our one-dimensional climate model runs reveal that the temperatures at which we observe those types of transport are predicted to occur at the Martian surface today and in the past. When scaled to Mars, the morphologies we observe with water and brine experiments should be resolvable using the High-Resolution Science Experiment (HiRISE) camera at ~25 cm/pix. Overall, our results show that boiling must be taken into account when considering sediment-rich flows under recent or current Martian conditions.

\* Corresponding author.

E-mail address: [philippe.meven@gmail.com](mailto:philippe.meven@gmail.com)

Postal address: 2 chemin de la Houssinière, 44300, Nantes (FRANCE)



Distributed under a Creative Commons Attribution | 4.0 International licence

## 1. Introduction

Whether water or brine has flowed recently over the Martian surface has been debated for decades as these fluids have been proposed to form gullies (Malin and Edgett, 2000; Figure 1a-c), recurring slope lineae (RSL; McEwen et al., 2011; Figure 1d-e) and slope streaks (Schorghofer et al., 2002; Figure 1f). This debate has been fuelled by the fact that water is vital for all life as we know it. Searching for signs of past or extant extraterrestrial life is one of the main objectives of space exploration programmes (e.g., Farley et al., 2020, Graf et al., 2002, Grotzinger et al., 2012, Schmidt, 2003, Zelenyi et al., 2015). However, what we know about Mars's current surface conditions makes it highly unlikely that enough stable liquid water is available to enable terrestrial-like water-driven mass-wasting processes (Haberle et al., 2001).

Liquid water is not thermodynamically stable at the surface of Mars (Haberle et al., 2001), because the air temperature and atmospheric pressure generally are too low ( $-60\text{ }^{\circ}\text{C}$  and 6 mbar on average), which means water is stable only in the form of ice or vapour. Hence, any liquid water on the surface would be in a metastable state. This condition means that small perturbations of temperature or vapour partial pressure of water ( $p[\text{H}_2\text{O}]$ ) would lead to freezing or boiling. For products other than pure water their vapour partial pressure ( $p[\text{H}_2\text{O}]$ ) can be related to their boiling temperature. For example, with salt in water, the higher the vapour pressure (at a given temperature) of the product, the lower its boiling temperature will be compared with a product with a lower vapour pressure at the same temperature. Salts have been detected on the surface of Mars and are widely distributed (Clark and Kounaves, 2016; Gasda et al., 2017; Gendrin, 2005; Hecht et al., 2009; Rivera-Valentín et al., 2020; Thomas et al., 2019). Therefore, liquid water at the surface would likely incorporate salt(s), forming a brine. This incorporation widens the domain of liquid stability of the solution, therefore brines would be more stable than pure water on the surface of Mars (Brass, 1980; Davila et al., 2010; Fischer et al., 2016; Rivera-Valentín et al., 2020).

Despite the existence of landforms that resemble terrestrial landforms formed from aqueous flows (e.g. gullies Malin and Edgett, 2000 or RSL McEwen et al., 2011) on the Martian surface, there is a lack of information on how that metastable water interacts with the substrate to engender sediment transport and to produce these landforms. In this context, several experimental studies have reported on sediment transport by water under Martian conditions (Massé et al., 2016; Raack et al., 2017; Herny et al., 2019), but only one has studied sediment transport by flowing brine (Massé et al., 2016). Massé et al. (2016) highlighted a new sediment transport process: grain ejection by boiling water and brine, brought about by the low atmospheric pressure and contact with "hot" sediment ( $>15\text{ }^{\circ}\text{C}$ ). In these experiments, brines were observed to transport less sediment by grain ejection than pure water. Massé et al. (2016), Raack et al. (2017) and Herny et al., (2019) all noted that boiling water was more efficient at transporting sediment than overland flows of stable water. Therefore, they proposed boiling as a way to solve the problem of the relatively large amount of water needed to form Martian features. These experiments also showed that the intensity of boiling-driven transport is determined by the temperature of the sediment the liquid is flowing over. However, Massé et al. (2016) only studied grain ejection, caused by seeping water and brine flows. Raack et al. (2017) and Herny et al. (2019) studied higher flow rates, but only used water. Therefore, this study aims at combining these two approaches by studying all the transport processes that boiling liquid can lead to, comparing the efficiency of both water and brine flows.

This study, therefore, pursues an experimental approach that:

1. follows the experimental protocol of Raack et al. (2017) and Herny et al. (2019) to expand the experimental dataset over a wider range of temperatures, which will lead to a better understanding of the processes at play beyond the known limits of the boiling phenomenon;
2. performs a comparative study (both qualitative and quantitative) of water and brine flows under Martian pressure at different sand temperatures, to understand how the type of liquid and the sand temperatures combine to drive the sediment transport.

First, we will describe our experimental setup and protocol as well as our data processing method. We will then present the results we obtained, followed by a discussion of the impact of our results on the potential for contemporary Martian aqueous flows.

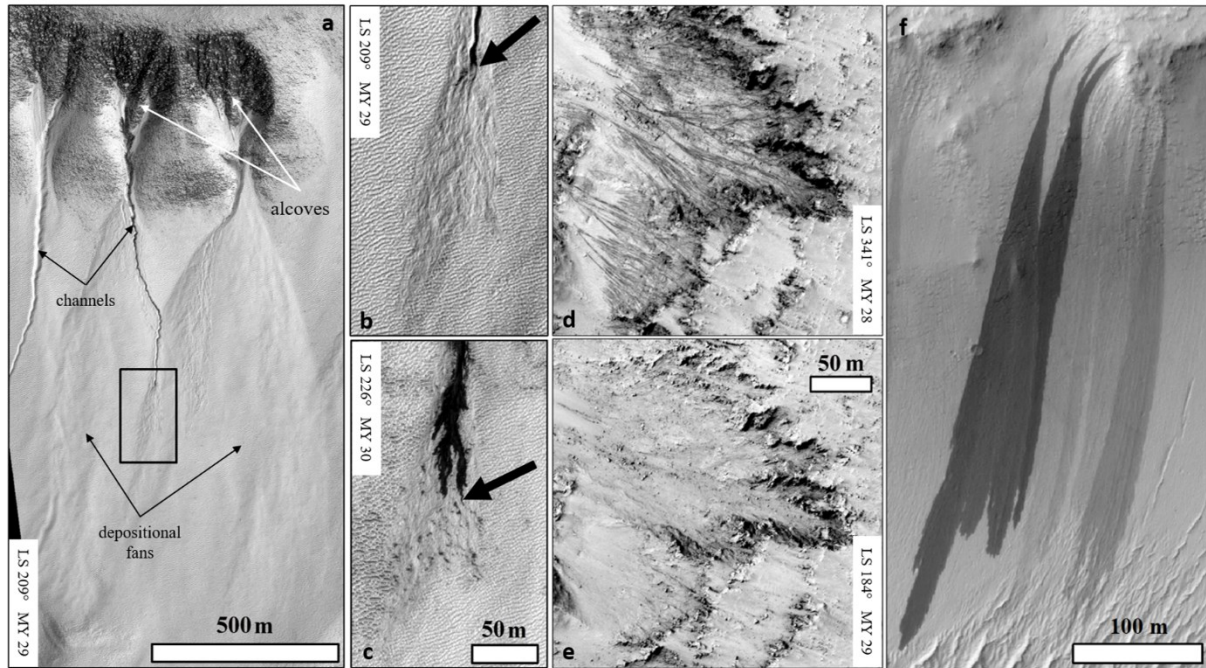


Figure 1: Recently active gullies, RSL and slope streaks. Solar Longitude ( $L_s$ ) is an angular value ( $0^\circ - 360^\circ$ ) giving the position of the planet on its orbit and thus indicates the season ( $L_s 0^\circ$  being the northern spring equinox). (a) Typical gully systems in Sisyphi Cavi ( $68.544^\circ\text{S}$ ,  $1.444^\circ\text{E}$ ) with alcoves, channels and depositional fans. The downslope direction is from top to bottom of the image and north is down. Taken from HiRISE image ESP\_011963\_1115. The black box delimits the extent of the images b & c. (b) and (c) Active depositional fan during the spring for Mars Year (MY) 29 and 30. Black arrows point to the terminus of the freshest deposits. Images b & c have the same scale and are taken from HiRISE images ESP\_011963\_1115 and ESP\_012319\_1115, respectively. (d) RSL originating from bedrock outcrops in the rim of Palikir Crater ( $41.65^\circ\text{S}$ ,  $157.705^\circ\text{W}$ ) in late summer in Mars Year 28. The downslope direction is from right to left of the image, and north is up. Taken from HiRISE image PSP\_005943\_1380. (e) RSL have faded by the early spring of the next Mars Year. Taken from HiRISE image ESP\_011428\_1380. Images d and e have the same scale. (f) Recent (darker) slope streaks, nearby more ancient (lighter) ones ( $0.148^\circ\text{N}$ ,  $36.840^\circ\text{E}$ ). Taken from HiRISE image ESP\_017605\_1800. Image credits: NASA/JPL/UofA.

## 2. Method

### 2.1. Protocol and setup

The experiments were performed in the Mars Simulation Chamber (MSC) at The Open University (Milton Keynes, UK), which provides an experimental environment at Mars-like pressures (e.g., Conway et al., 2011; Herny et al., 2019; Massé et al., 2016; Raack et al., 2017; Sylvest et al., 2016, 2019).

For each experiment, we placed a levelled-out sand bed of 5 cm depth in a rectangular tray (90x40 cm) inclined at  $25^\circ$ . We chose this angle to be consistent with the experiments of Raack et al. (2017) and Herny et al. (2019). Moreover, Martian features such as gullies and RSL are commonly found on slopes with similar angles (Heldmann and Mellon, 2004; Dickson et al., 2007; McEwen et al., 2011; Ojha et al., 2014). Each experiment began with depressurisation of the MSC using a vacuum pump, with the pressure maintained at  $\sim 7$  mbar. A water pump transferred 550 to 600 g of liquid (water or  $\text{MgSO}_4$  brine at 19 wt%), in one minute, from a reservoir outside the MSC to an outlet 5 cm above the sand bed (Figure 2). As liquid temperature only had a minor influence on experiments by Herny et al. (2019), water and brine were always at ambient temperature in the reservoir ( $19.7 \pm 2.5^\circ\text{C}$ ). We performed three replicates of five sand temperatures: 0, 5, 15, 17.5 and  $20^\circ\text{C}$ . The sand was stored in a freezer before the experiment and was left to warm at room temperature in the MSC. The sand temperature was not maintained, and hence increased during the experiments but at a very slow rate ( $0.2^\circ\text{C}$  on average along the experiments). We started the depressurisation just before the target sand temperature was

reached, and started the flow when the target sand temperature and the target pressure were both reached. When no further motion was observed inside the MSC, we repressurised the MSC and stopped the experiment.

The sand used was sieved and was composed of grains with diameters from 125  $\mu\text{m}$  to 450  $\mu\text{m}$  ( $\sim 96$  wt%), with a median diameter of 250-300  $\mu\text{m}$ . This fractionation is within the range of grain sizes observed on Mars' surface (Rivera-Hernández et al., 2019; Squyres et al., 2004; Weitz et al., 2018). We chose a  $\text{MgSO}_4$  brine (the freezing point at eutectic is about  $-3.5$   $^\circ\text{C}$ ; Brass, 1980) because this salt is common on Mars (Gendrin, 2005). Moreover it is easy to acquire, and no specific precautions have to be taken to work with it. Twelve photogrammetric targets were located at different heights along the edges of the tray (Figure 3). Fifteen thermocouples recorded temperatures (time step = 1 s) at the following locations: eight at the base of the sand layer along the middle of the tray; four on 2.5-cm-high pillars within the sand bed; one at the surface of the sand; one in the liquid outlet; one in the liquid reservoir outside the MSC (Figure 3). Inside the MSC, there was one Pirani pressure gauge to record inner pressure (time step = 1 s), an ibutton sensor recording air temperature and relative humidity (time step = 1 s), and two webcams. Outside the MSC there was one high-resolution video camera which was used to record each experiment. All devices were recording/monitoring from before the depressurisation until after the repressurisation. The protocol that we employed has been used by Raack et al. (2017) and Herny et al. (2019) (with water flows only).

To summarise, the parameters we varied from one experiment to the other were the sand temperature (0, 5, 15, 17.5 and 20  $^\circ\text{C}$ ) and the type of liquid (water or  $\text{MgSO}_4$  brine at 19 wt%). The slope angle and the pressure were kept constant. We monitored the relative humidity, liquid temperature, and air temperature, but did not attempt to control them.

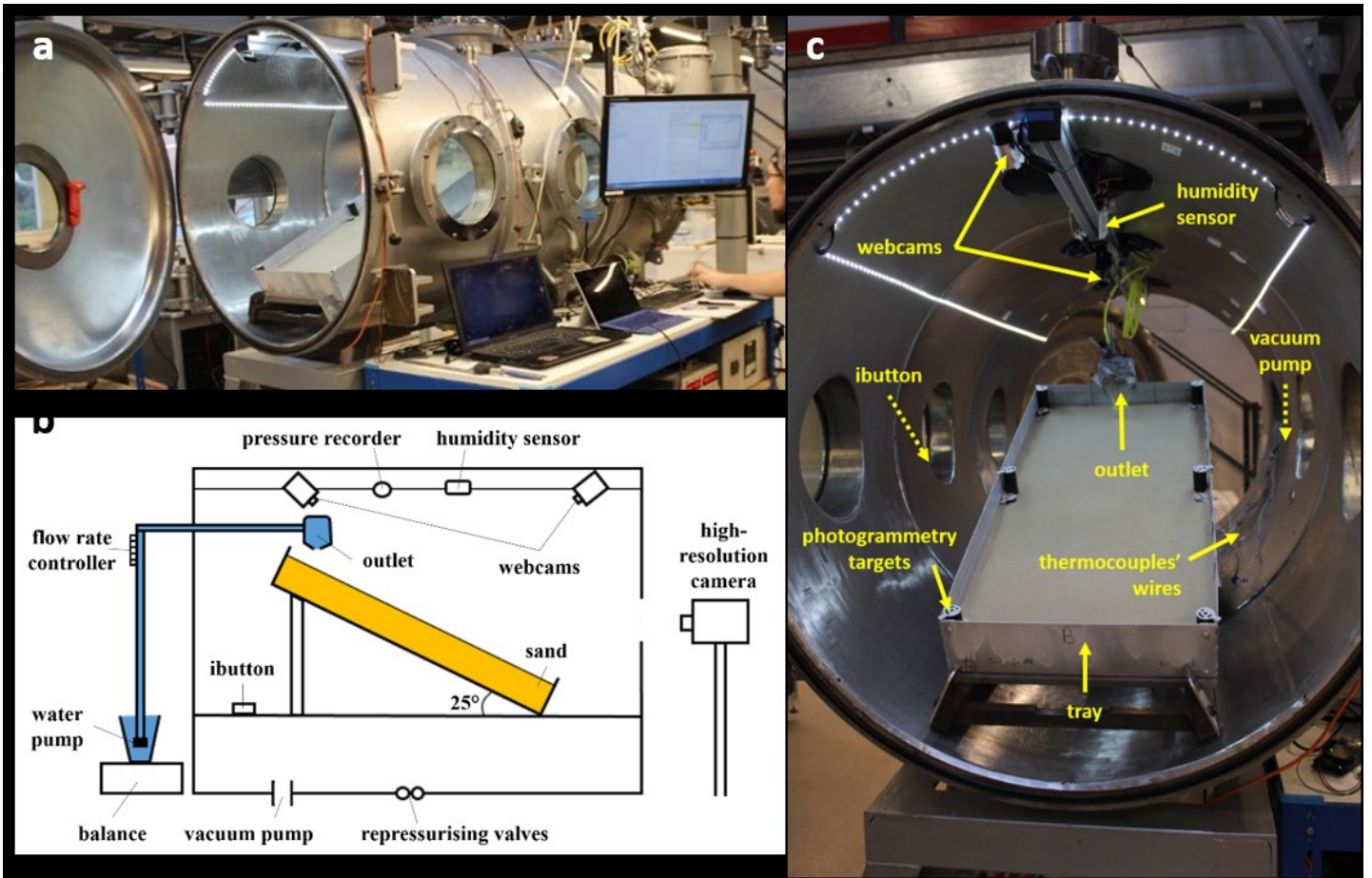


Figure 2: **a.** photograph of the outside of the MSC with the tray visible through the open door; **b.** schematic of the MSC. The “ibutton” is a temperature and humidity sensor; **c.** annotated photograph of the MSC interior showing the positions of the main pieces of equipment. Dashed lines point to devices that are hidden in this photograph. The MSC is approximately 2 m long and 0.9 m in diameter.

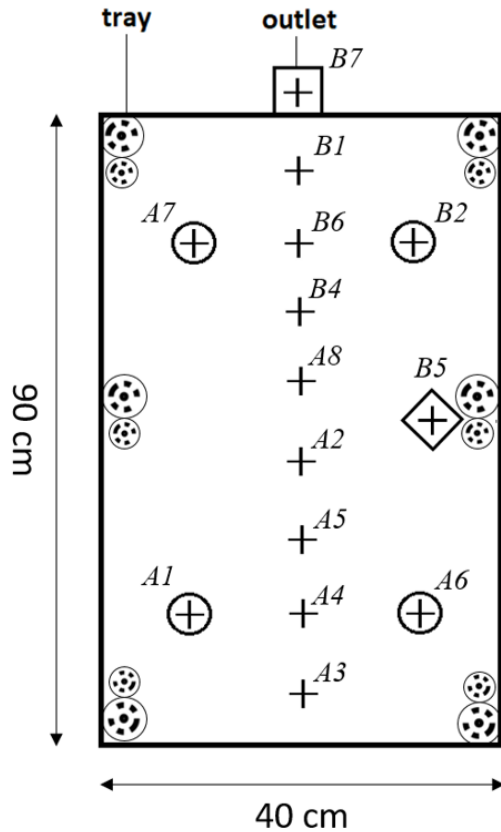


Figure 3: Top-down schematic of the experimental tray with the position of the 15 thermocouples in the tray, labelled as they are in the software and in the Supplementary Table S1. Crosses represent the thermocouples at the base of the sand bed, circled crosses represent the thermocouples within the sand bed on pillars at 2.5 cm above the base of the tray and the diamond-cross represents the thermocouple at the surface of the sand bed. The twelve photogrammetric targets attached to the tray are also located on the sketch.

## 2.2. Data processing

### 2.2.1. Analysis of morphologies and volumes

Similarly to Raack et al. (2017) and Herny et al. (2019), we used Agisoft Photoscan (version 1.3) software to create Digital Terrain Models (DTMs) at 1 mm/pixel and orthomosaics at 0.2 mm/pixel from series of 100-150 photographs of the sand bed (Structure from Motion technique - Bolles et al., 1987; Westoby et al., 2012). The photographs were taken before and after each experiment with a handheld commercial camera (Casio EX-FH20 - 9 Mpixel, focal length = 5 mm). The software aligns the photographs by recognising the overlapping parts and calculates the scale using the user-input coordinates of the photogrammetric targets. For each experiment, we obtained two DTMs and two orthomosaics of the sand bed, before and after the flow (Figure 4a & b). A hillshaded relief image for each DTM was produced using ArcGIS (version 10.4). The difference between the values of the DTMs after and before (DTM of difference - DoD, e.g., Herny et al., 2019; Morino et al., 2019, 2021; Williams, 2012; Raack et al., 2017) was computed in order to visualise the erosion zones (negative values) and the deposition zones (positive values), and to calculate the volume of sediment moved during each experiment (DoDs available in Supplementary Files).

We observed four different sediment transport processes: overland flow (the liquid flowing at the surface of the sand bed, carrying sediment); percolation (the liquid infiltrating within the sand bed around the point of liquid supply); boiling (the liquid changing to gas phase on the sand bed, leading to grain ejection; Massé et al., 2016); and “levitation” (liquid-saturated pellets of sand and changing to the gas phase, leading to these pellets to move downslope quickly, supported by cushions of water vapour; Raack et al., 2017).

Based on the observation of those four processes and on the surface morphology of the sand bed after the experiments, we identified six different landforms (six “morphological units”; [Figure 4b](#)):

- unit 1: the channel and its associated deposits. The channel is a few centimetres wide and deep, it originates from a pit located right below the water supply and extends downslope. The sediment that was initially filling the channel is found at its terminus, deposited downslope as several tongues of sediment – similarly to an alluvial fan. Channel and associated deposits form by overland flow, progressively, from the liquid supply point;
- unit 2: the saturated zone. It is a volume of sand around the liquid supply point which is water-saturated and appears darker. The channel and often its associated deposits (unit 1) overprint the saturated zone and, when applicable, the saturated zone lays at the bottom of the depression (unit 3). The saturated zone forms by the progressive percolation of water through the sand bed during the experiments;
- unit 3: the depression and its associated avalanche deposits. The depression is a pit located below the liquid supply, around ten centimetres deep and extending radially for tens of centimetres; the saturated zone is at its base. The sediment initially filling the depression forms avalanche deposits, elongated positive relief features found downslope the depression, 10 to 20 centimetres wide and up to nearly one metre long. The depression and associated avalanche deposits are formed by boiling water. Boiling is first observed at the liquid supply point when liquid encounters the relatively hot sand bed. It then follows the edges of the growing saturated zone (unit 2). This continuous process ejects sand grains downslope, which progressively forms the depression within the sand bed around the saturated zone, and associated avalanche deposits downslope;
- unit 4: the pellets. They are pellets of water-saturated sediment, of maximum a few centimetres wide and long. They are located downslope, often far away from the liquid supply point – most of them being found in the lowest ~ quarter of the tray. They form at the very beginning of the experiments by “levitation”: the water they contain undergoes a phase change from liquid to gas, which generates a cushion of vapour between the pellet and the sand bed, allowing it to move downslope quickly;
- unit 5: the fine deposits. They are a thin layer of the finest grain sizes of the sand we use, and are located around the depression and avalanche deposits (unit 3). They form by boiling, which ejects fine grains further than the avalanche deposits;
- unit 6: the covered pellets. They are regular pellets, but they were covered during the experiments by avalanche deposits (unit 3).

Units 1 to 4 are consistent with those defined by Raack et al. (2017) and Herny et al. (2019); we added units 5 and 6.

To estimate the volume of sediment moved within each unit, we mapped them individually for each experiment (outlines available in Supplementary Files), using the hillshaded reliefs, the orthomosaics and videos of the experiment. For unit 6 we only used the video recordings to map its extent, because this unit was buried during the experiment. First, for each pellet, we used recordings from different angles to estimate its height. Then we chose a frame of the video when the pellet had formed, but was not moving anymore and had not yet been covered by the avalanche deposits. We projected that frame onto the corresponding orthomosaic and proceeded with the mapping.

The volumes of sediment deposited within each unit were calculated for each experiment using the DoD. The total volume transported was the sum of the volumes of sediment deposited within each unit. The volume of the saturated zone (unit 2), pellets (unit 4) and fine deposits (unit 5) were simply the deposited volumes within these units. The volumes of covered pellets (unit 6) were obtained by multiplying the area of each pellet by their height (previously estimated – see above). The overall volume of pellets was the sum of the volumes of the visible pellets (unit 4) and covered pellets (unit 6). The volumes of the avalanche deposits were the deposited volumes within unit 3 (which comprises the depression and avalanche deposits), from which were subtracted the volumes of covered pellets (unit 6).

To provide a realistic estimate of the volume mobilised by overland flow (unit 1), we needed to topographically isolate this unit to remove the influence of the depression caused by the ejection of saltation deposits (unit 3). To do this we created a “reference DTM” for unit 1 that roughly described the surface over which the liquid flowed. To construct this reference DTM we extracted the elevation

values within a 0.5 cm buffer around the exterior of the polygon describing the unit 1. These values were used to interpolate the values within the area of unit 1 using a Natural Neighbour algorithm. By computing the difference between the “after” DTM and the new reference DTM we estimated the erosion and deposition volumes for unit 1 (overland flow), being respectively the volume of runoff channel and the volume of runoff deposits. Length and width of the channels and deposits also were measured manually in ArcGIS, the length being considered as the distance between the liquid supply point and the point of the deposits that are the furthest downslope (digitised as a broken line following the middle of the channel and deposits as much as possible), and width is considered as the distance between the two high points at the very top of the channel, itself located at the base of the depression (unit 3).

To calculate the uncertainty in the calculation of the volumes transported derived from the DTMs, we drew a “reference polygon” (a square of ~ 5 to 15 cm side depending on the available space) for each experiment in an area where we could not see any sand movement using the orthomosaics and the hillshaded relief images (Raack et al., 2017; Herny et al., 2019). Using the DoD we calculated the eroded and deposited volume within the reference polygon per unit area (which if the DTMs were perfect should equal zero). We estimated the potential error for the depositional and erosional volumes derived for each unit by scaling this error to their areas. For unit 6 (covered pellets), we estimated the error on the height at 0.2 cm and multiplied it by the area of the unit. The uncertainty on the total volume of pellets hence is the resulting value, summed with the error on visible pellets calculated with the reference polygon.

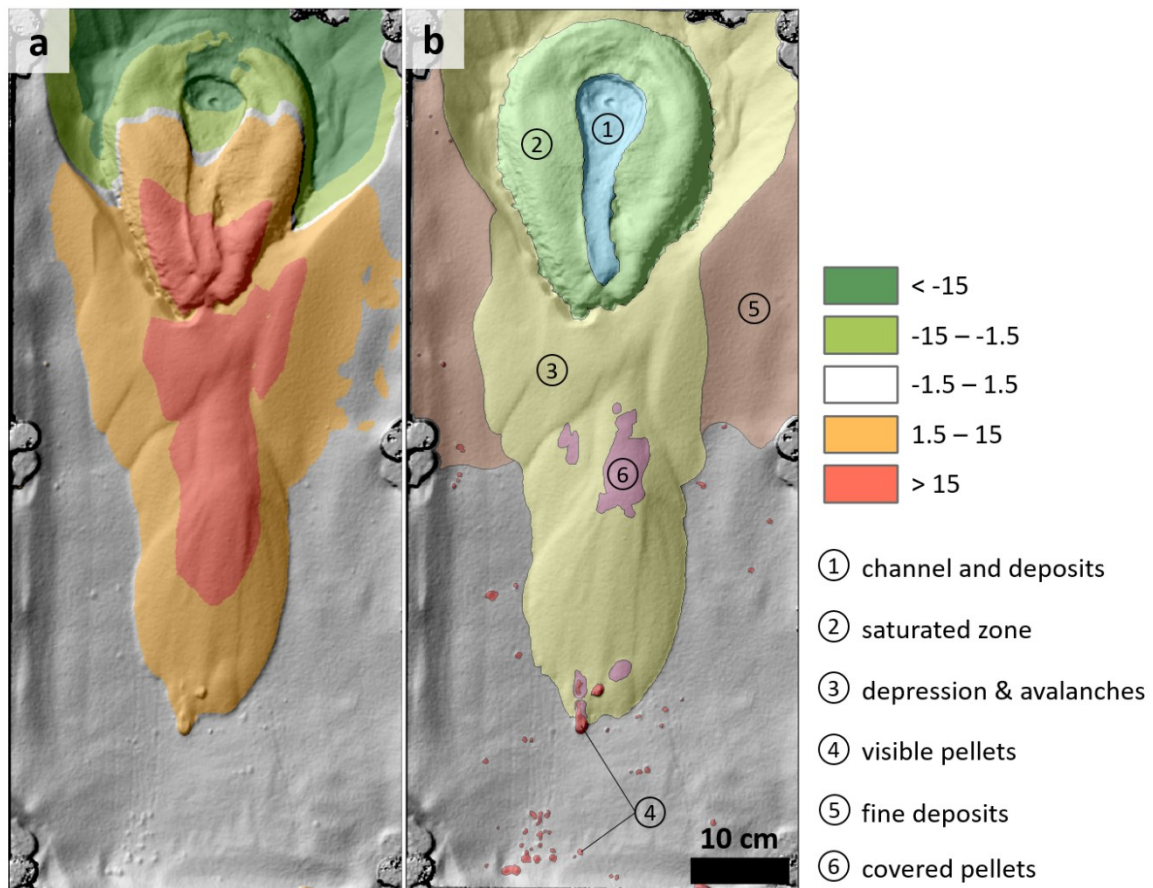


Figure 4: Example of the experiment 01. **a.** The hillshaded DTM after the experiment, overlain by the zones of erosion (blue) and of deposition (red). The legend is expressed in millimetres. **b.** The hillshaded DTM after the experiment, overlain by the polygons representing the different units used to estimate the volumes moved by each process: the channel and deposits formed by overland flow (unit 1); the saturated zone formed by water percolation (unit 2); the depression and avalanche deposits resulting from grain ejection by boiling (unit 3); the visible pellets, formed by “levitation” of sand on cushions of vapour (unit 4); the fine deposits resulting from fine grain ejection by boiling (unit 5); the pellets covered by the avalanche deposits (unit 6).

### 2.2.2. Physical parameters

To understand which parameters were controlling the transport processes we observed, we first identified the transport period for each run, i.e. the time interval between the start of liquid release and the end of visible movements on the video. Then, we calculated the mean and standard deviation (to account respectively for the values and variability associated with each run) of pressure, air temperature, relative humidity, liquid temperature and surface temperature over this time period (full records available in Supplementary Table S1). The error of the air temperature is the accuracy of the sensor, i.e. 0.5 °C. The sand temperature was calculated using all the data from the four thermocouples located within the sand bed. The mass of liquid used is the difference between the weight of the liquid container immediately before and immediately after the liquid flowed, with an accuracy of 5 g. The length and width of the channels have been estimated with 1 cm and 5 mm uncertainty, respectively.

### 2.3. Scaling

In the following subsections we summarise the calculations made by Massé et al. (2016) and Raack et al. (2017) to scale their experiments to the lower Martian gravity compared to their experiments. We use their results to perform our own scaling calculations presented in [Section 4.3](#).

#### 2.3.1. Grain ejection by boiling (Massé et al., 2016)

Massé et al. (2016) performed experiments of flowing water within sand beds under Martian pressure (6.5 to 9 mbar), and they also observed sand grain ejection due to water boiling. They calculated the gas speed expected during their experiments, from an adapted equation initially created to calculate phase change gas speed in capillary tubes (Massé et al., 2016 in Supplementary Discussion). They then created a numerical model to simulate the grain initial acceleration and ballistic trajectory under the reduced Martian gravity, with the gas speed previously calculated. They conclude that the reduced gravity results in a higher initial grain ejection speed compared to Earth, inducing a travel distance 2.5 to 3 times greater on Mars than on Earth.

#### 2.3.2. Pellet “levitation” (Raack et al., 2017)

Raack et al. (2017) performed experiments of water flows over sand beds, with the same setup as the present article. They observed, among other processes, formation of pellets by “levitation” that we also observe during our experiments (see [Section 2.2.1](#)). To estimate how efficient the “levitation” force would be under the reduced Martian gravity, they calculated and compared two opposing forces over time: the friction force (inhibiting the pellet sliding downslope) and the levitation force (favouring the pellet sliding downslope). They stated that pellets can “levitate” only if the levitation force overcomes the friction force – i.e. if the ratio [levitation force]/[friction force] is  $> 1$ . Therefore, they studied those forces in the scope of the reduced Martian gravity, and concluded that the friction force would be lower on Mars, resulting in pellets sliding for a time up to 48 times longer.

## 3. Results

We performed a total of 33 experiments involving ten combinations with the two types of liquids (water and magnesium sulphate brine at 19 wt%) and five sand temperatures (0, 5, 15, 17.5 and 20 °C; [Table 1](#)). Runs 19 and 33 are not taken into account in the results and do not appear in [Table 1](#) because of operator error: pressure that went too low and sand temperature too high (run 19), and a too-rapid depressurisation that caused an avalanche before the liquid release (run 33). A triplicate of each combination was our aim but the difficulty in always obtaining the same average surface temperatures caused deficits or additions in some series ([Table 1](#)). We separate the experiments into two groups, based on the occurrence of boiling or not: “hot” (15 to 20 °C, where boiling occurs) and “cold” (0-5 °C, where boiling is minimal). In the following section we present first the transport processes that we observed during the experiments, and then the quantification of these processes on both “hot” and “cold” sediment. Supplementary Videos show four typical experiments combining hot or cold sand and water or brine.

Supplementary Table S1 shows the physical parameters measured in each experiment, with the full records of sand temperature, air temperature & pressure and relative humidity for the duration of the experiments.

### *3.1. Observations on transport processes*

Consistent with the results reported by Massé et al. (2016), Raack et al. (2017) and Herny et al. (2019), we observed intense boiling of both water and brine due to the low pressure, with sediments from 10 °C to 20 °C (“hot experiments”, [Figure 5](#)). With sediments from 0 °C to 5 °C (“cold experiments”), the boiling manifested itself in bubble formation visible at the surface of the flows and was not intense enough to induce sediment movement by ejection. We observed several processes that are known on Earth: formation of erosion channels and subsequent deposits by overland flow, and sediment saturation by percolation. However several processes were caused by the phase change of water from liquid to gas, and so are unknown in natural settings on Earth: i. grain ejection forming a depression at the source, avalanche deposits along the sand bed and fine deposits layers on the sides (Massé et al., 2016; [Figure 5](#)); ii. downslope movement of wet sand pellets, levitating on cushions of vapour formed by boiling of the water they contain (Raack et al., 2017; [Figure 6](#)); and iii. mm-sized pellet ejection around the saturated zone. All of these processes (overland flow, percolation, boiling, “levitation”) occur on hot sediments (10 °C to 20 °C). On colder sediment (0 °C to 5 °C) only overland flow, percolation and mm-sized pellet ejection are observed ([Figure 7](#), [Figure 8](#); , [Supplementary Videos](#)). These differences in terms of active processes lead to important differences in terms of morphology between cold and hot experiments.

| run | type of liquid | water weight (g) | sand temperature (°C) | air temperature (°C) | pressure (mbar) | relative humidity (%) | runoff length (cm) | runoff width (cm) | strong saltation duration (s) | total volume transported | transported volumes (cm <sup>3</sup> ) |                       |                      |                   |
|-----|----------------|------------------|-----------------------|----------------------|-----------------|-----------------------|--------------------|-------------------|-------------------------------|--------------------------|----------------------------------------|-----------------------|----------------------|-------------------|
|     |                |                  |                       |                      |                 |                       |                    |                   |                               |                          | volume of overland flow                | volume of percolation | volume of avalanches | volume of pellets |
| 1   | water          | 625 ± 5          | 20.38 ± 0.12          | 19.38 ± 0.5          | 8.48 ± 0.62     | 26.99 ± 10.59         | 21.54 ± 1          | 4.27 ± 0.5        | 103 ± 3                       | 1355.1 ± 11.5            | 55.9 ± 0.1                             | 300.5 ± 0.4           | 936.1 ± 1.4          | 62.6 ± 9.6        |
| 2   | water          | 570 ± 5          | 20.43 ± 0.11          | 20.11 ± 0.5          | 8.3 ± 0.67      | 33.12 ± 6.62          | 21.84 ± 1          | 5.55 ± 0.5        | 107 ± 3                       | 1300.9 ± 16.3            | 71.1 ± 0.1                             | 174.4 ± 0.4           | 837 ± 2.2            | 218.3 ± 13.6      |
| 3   | water          | 605 ± 5          | 20.85 ± 0.11          | 20.35 ± 0.5          | 8.6 ± 0.71      | 32.13 ± 10.05         | 23.32 ± 1          | 5.23 ± 0.5        | 107 ± 3                       | 2064.2 ± 29.7            | 89.3 ± 0.1                             | 176.6 ± 0.5           | 1578.8 ± 3.7         | 219.5 ± 25.4      |
| 4   | brine          | 560 ± 5          | 19.08 ± 0.12          | 18.54 ± 0.5          | 7.99 ± 0.42     | 27.91 ± 9.36          | 22.52 ± 1          | 2 ± 0.5           | 76 ± 3                        | 784.4 ± 10.1             | 31.9 ± 0                               | 187.7 ± 0.6           | 489.6 ± 1.4          | 75.2 ± 8.1        |
| 5   | brine          | 575 ± 5          | 20.89 ± 0.12          | 20.19 ± 0.5          | 8.24 ± 0.52     | 28.16 ± 8.2           | 28.38 ± 1          | 2.68 ± 0.5        | 99 ± 3                        | 1101.6 ± 51.9            | 62.2 ± 0.2                             | 93 ± 1.2              | 729.7 ± 7.6          | 216.8 ± 42.8      |
| 6   | brine          | 595 ± 5          | 20.19 ± 0.09          | 18.54 ± 0.5          | 8.3 ± 0.53      | 26.22 ± 11.18         | 43.2 ± 1           | 4.07 ± 0.5        | 94 ± 3                        | 883.4 ± 19.3             | 142.5 ± 1.1                            | 113.5 ± 1.1           | 554.7 ± 5.1          | 72.7 ± 12         |
| 7   | brine          | 565 ± 5          | 5.06 ± 1.27           | 20.38 ± 0.5          | 7.83 ± 0.61     | 27.24 ± 5.66          | 34.96 ± 1          | 1.64 ± 0.5        | /                             | 91.1 ± 3.9               | 76.7 ± 2.3                             | 5.9 ± 1               | /                    | 8.5 ± 0.6         |
| 8   | brine          | 600 ± 5          | 5.09 ± 1.13           | 18.54 ± 0.5          | 8.21 ± 0.22     | 16.81 ± 6.2           | 40.66 ± 1          | 1.47 ± 0.5        | /                             | 75.1 ± 1.9               | 70.2 ± 1.2                             | 1.9 ± 0.3             | /                    | 3.1 ± 0.4         |
| 9   | brine          | 590 ± 5          | 4.88 ± 0.74           | 18.54 ± 0.5          | 8.19 ± 0.28     | 16.47 ± 5.49          | 35.29 ± 1          | 2.16 ± 0.5        | /                             | 68.5 ± 1.7               | 62.3 ± 1.2                             | 3.8 ± 0.3             | /                    | 2.4 ± 0.2         |
| 10  | brine          | 580 ± 5          | 15.65 ± 0.13          | 14.35 ± 0.5          | 8 ± 0.41        | 14.21 ± 6.91          | 39.14 ± 1          | 2.66 ± 0.5        | 47 ± 3                        | 668.1 ± 12.2             | 75.5 ± 0.3                             | 190.8 ± 1.2           | 326.3 ± 1.7          | 75.5 ± 9          |
| 11  | brine          | 595 ± 5          | 16.08 ± 0.1           | 14.54 ± 0.5          | 8.2 ± 0.48      | 23.83 ± 9.65          | 38.86 ± 1          | 2.71 ± 0.5        | 98 ± 3                        | 959.1 ± 19.3             | 76.9 ± 0.5                             | 286.8 ± 1.9           | 557 ± 4.6            | 38.4 ± 12.3       |
| 12  | brine          | 595 ± 5          | 16.27 ± 0.17          | 14.54 ± 0.5          | 8.18 ± 0.3      | 24.3 ± 11.69          | 40.12 ± 1          | 2.93 ± 0.5        | 69 ± 3                        | 782 ± 15.6               | 95.4 ± 0.9                             | 198.2 ± 1.8           | 424.2 ± 5            | 64.1 ± 7.9        |
| 13  | water          | 590 ± 5          | 14.85 ± 0.14          | 12.8 ± 0.5           | 8.12 ± 0.25     | 30 ± 13.73            | 22.79 ± 1          | 3.7 ± 0.5         | 97 ± 3                        | 878.9 ± 13.4             | 72.1 ± 0.5                             | 168 ± 1.3             | 603.3 ± 4.3          | 35.5 ± 7.3        |
| 14  | water          | 585 ± 5          | 15.51 ± 0.14          | 13.54 ± 0.5          | 8.09 ± 0.29     | 31.61 ± 12.95         | 22.56 ± 1          | 4.23 ± 0.5        | 116 ± 3                       | 494.5 ± 10.2             | 52.2 ± 0.5                             | 134.9 ± 2             | 285.3 ± 4.1          | 22.1 ± 3.7        |
| 15  | water          | 590 ± 5          | 15.54 ± 0.14          | 14.35 ± 0.5          | 7.99 ± 0.51     | 34.18 ± 11.04         | 21.19 ± 1          | 3.99 ± 0.5        | 113 ± 3                       | 980.6 ± 8.9              | 58.2 ± 0.2                             | 130.1 ± 0.8           | 774.8 ± 3            | 17.4 ± 4.8        |
| 16  | water          | 595 ± 5          | 5.06 ± 0.41           | 16.36 ± 0.5          | 7.8 ± 0.17      | 23.34 ± 7.57          | 26.26 ± 1          | 4.08 ± 0.5        | /                             | 65.3 ± 0.7               | 49.7 ± 0.3                             | 13.7 ± 0.3            | /                    | 1.9 ± 0.1         |
| 17  | water          | 600 ± 5          | 10.12 ± 0.72          | 18.45 ± 0.5          | 8.12 ± 0.5      | 19.37 ± 8.87          | 24.91 ± 1          | 3.61 ± 0.5        | 92 ± 3                        | 474.5 ± 8                | 65.4 ± 0.8                             | 67.8 ± 1.2            | 334 ± 3.8            | 7.3 ± 2.2         |
| 18  | water          | 595 ± 5          | 5.23 ± 1.14           | 18.04 ± 0.5          | 7.95 ± 0.31     | 24.12 ± 6.62          | 27 ± 1             | 3.54 ± 0.5        | /                             | 60.9 ± 1.3               | 51.6 ± 0.6                             | 8.4 ± 0.6             | /                    | 0.9 ± 0.1         |
| 20  | brine          | 565 ± 5          | -0.37 ± 1.26          | 18.45 ± 0.5          | 7.09 ± 0.08     | 19.48 ± 4.91          | 40.77 ± 1          | 1.99 ± 0.5        | /                             | 54.4 ± 4.2               | 52.5 ± 2.9                             | 0.6 ± 0.4             | /                    | 1.3 ± 0.8         |
| 21  | brine          | 545 ± 5          | 0.24 ± 1.71           | 18.37 ± 0.5          | 7.23 ± 0.24     | 18.66 ± 4.02          | 42.82 ± 1          | 1.64 ± 0.5        | /                             | 55 ± 1.9                 | 52.5 ± 1.4                             | 0.8 ± 0.1             | /                    | 1.6 ± 0.4         |
| 22  | water          | 590 ± 5          | -0.11 ± 1.96          | 18.37 ± 0.5          | 7.34 ± 0.28     | 18.12 ± 4.73          | 27.14 ± 1          | 3.03 ± 0.5        | /                             | 75.8 ± 1.9               | 72 ± 1.2                               | 3.1 ± 0.4             | /                    | 0.7 ± 0.3         |
| 23  | water          | 590 ± 5          | -0.35 ± 1.59          | 18.37 ± 0.5          | /               | 20.73 ± 5.25          | 28.31 ± 1          | 2.7 ± 0.5         | /                             | 78 ± 0.7                 | 73.2 ± 0.4                             | 3.9 ± 0.2             | /                    | 0.9 ± 0.1         |
| 24  | water          | 600 ± 5          | 0.09 ± 1.08           | 17.54 ± 0.5          | 7.25 ± 0.23     | 21.48 ± 4.77          | 27.57 ± 1          | 4.5 ± 0.5         | /                             | 84.2 ± 5.8               | 70.8 ± 2                               | 12.7 ± 3.5            | /                    | 0.7 ± 0.3         |
| 25  | water          | 585 ± 5          | 17.32 ± 0.13          | 15.54 ± 0.5          | 7.69 ± 0.54     | 30.94 ± 10.44         | 25.64 ± 1          | 2.67 ± 0.5        | 106 ± 3                       | 1331.9 ± 16.7            | 73.2 ± 0.4                             | 272.9 ± 1.9           | 952.7 ± 6            | 33.1 ± 8.4        |
| 26  | water          | 590 ± 5          | 15.82 ± 1.42          | 15.86 ± 0.5          | 7.79 ± 0.47     | 29.16 ± 10.1          | 26.24 ± 1          | 3.43 ± 0.5        | 92 ± 3                        | 1032.7 ± 12              | 85.2 ± 0.3                             | 213.4 ± 0.8           | 688.1 ± 2.4          | 46 ± 8.5          |
| 27  | water          | 595 ± 5          | 17.55 ± 0.1           | 15.68 ± 0.5          | 7.86 ± 0.55     | 29.07 ± 11.46         | 20.78 ± 1          | 4.41 ± 0.5        | 101 ± 3                       | 1288.4 ± 12.6            | 74.2 ± 0.2                             | 335 ± 1.2             | 830.4 ± 3.8          | 48.7 ± 7.4        |
| 28  | water          | 595 ± 5          | -0.4 ± 1.64           | 15.36 ± 0.5          | 6.89 ± 0.2      | 29.19 ± 5.01          | 27.98 ± 1          | 2.32 ± 0.5        | /                             | 80.2 ± 4.8               | 77.8 ± 3.9                             | 2.3 ± 0.7             | /                    | 0.1 ± 0.2         |
| 29  | brine          | 555 ± 5          | 17.15 ± 0.16          | 17.96 ± 0.5          | 7.71 ± 0.55     | 22.93 ± 9.78          | 35.34 ± 1          | 2.73 ± 0.5        | 93 ± 3                        | 768.6 ± 11.8             | 61.3 ± 0.2                             | 223.4 ± 1.1           | 410.3 ± 2.7          | 73.6 ± 7.9        |
| 30  | brine          | 590 ± 5          | 17.52 ± 0.08          | 16.54 ± 0.5          | 7.55 ± 0.38     | 27.42 ± 9.42          | 37.49 ± 1          | 2.4 ± 0.5         | 89 ± 3                        | 918 ± 13.4               | 105.2 ± 0.8                            | 147.7 ± 1.3           | 558.6 ± 5.2          | 106.5 ± 6.1       |
| 31  | brine          | 590 ± 5          | 17.17 ± 0.22          | 16.36 ± 0.5          | 7.74 ± 0.54     | 27.67 ± 9.81          | 22.89 ± 1          | 1.76 ± 0.5        | 92 ± 3                        | 873.3 ± 9                | 25.5 ± 0.1                             | 283.3 ± 1.6           | 486.3 ± 3.1          | 78.1 ± 4.2        |
| 32  | brine          | 585 ± 5          | 0.67 ± 1.04           | 17.54 ± 0.5          | 7.29 ± 0.26     | 20.34 ± 4.8           | 45.07 ± 1          | 1.43 ± 0.5        | /                             | 68.3 ± 1.4               | 66.9 ± 1                               | 0.7 ± 0.2             | /                    | 0.7 ± 0.2         |

Table 1: summary of parameters and measurements for each run

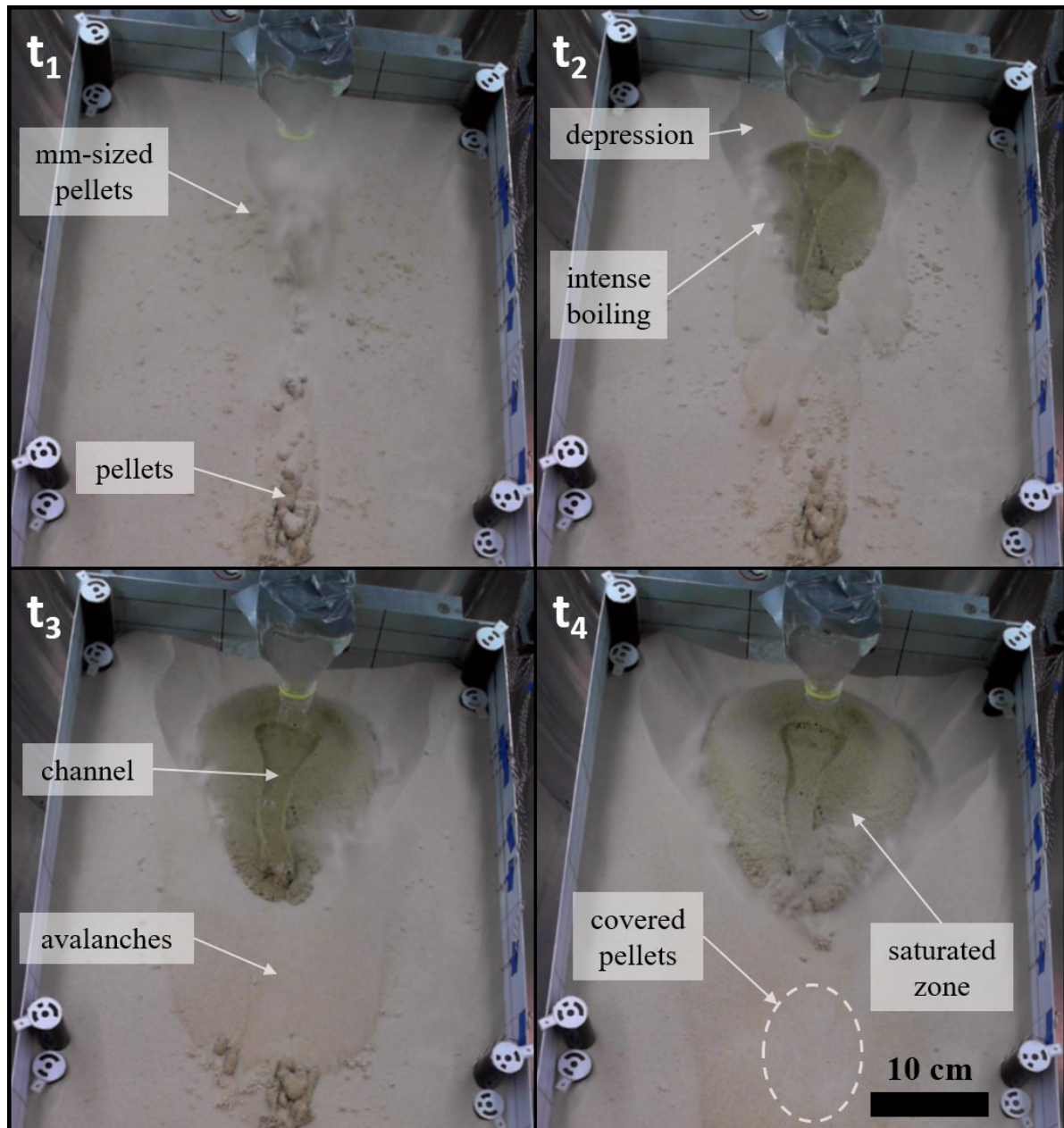


Figure 5: images of the top of the sand bed from the webcam recording of experiment 01 (water, 20 °C) at  $t_1=5$  s,  $t_2=30$  s,  $t_3=60$  s,  $t_4=90$  s after the beginning of the experiment. We observe the progressive formation of the channel, the saturated zone and the depression/avalanche deposits. Note that the pellet “levitation” occurs within the very first seconds of the experiment.

Experiments with water and brine flow both showed the same transport processes and sequences of events, which are described in the following text. Experiments with hot sediment begin with pellet “levitation” immediately after the liquid comes into contact with the sand (Figure 6), and mm-sized pellets are ejected at the same time (Figure 5). Intense boiling starts immediately after the first pellets are ejected (Figure 5), and in a few seconds a depression starts forming. Percolation starts immediately after the first few tenths of a second of boiling and forms a growing saturated zone; there is no further pellet “levitation” or ejection. Some small avalanche deposits start forming. Overland flow forms channels and deposits after a few tens of seconds, when the saturated zone is already several centimetres wide. After that, we observed a slow but continuous decrease in boiling intensity, and the boiling can last from 45 s to nearly 2 min (extending after the one-minute-long liquid release has stopped); the

depression continues to get bigger and the avalanche deposits longer and wider; the percolation progresses and makes the saturated zone grow continuously during the one-min flow; channel and deposits become longer and wider. Avalanche deposits can cover some pellets during their progression (Figure 5).

Cold sediment experiments immediately start with overland flow forming channels and deposits (Figure 8). Some small pellets levitate over a few centimetres but will be covered by the flow deposits before the end of the experiment. The percolation starts forming a saturated zone around the channel, which progressively gets longer and wider. Channel deposits extend, and spread to form a depositional fan. Bubbles formed by boiling are visible at the surface of the flow. Millimetre-sized pellets are ejected throughout the experiment when bubbles explode. The overland flow stops when the liquid release stops, but the percolation continues (Figure 8).

It should be noted that some morphologies can overlap other ones. As an example, avalanche deposits form constantly during the hot experiments and they cover pellets most of the time since those are preferentially formed at the very beginning of the hot experiments.

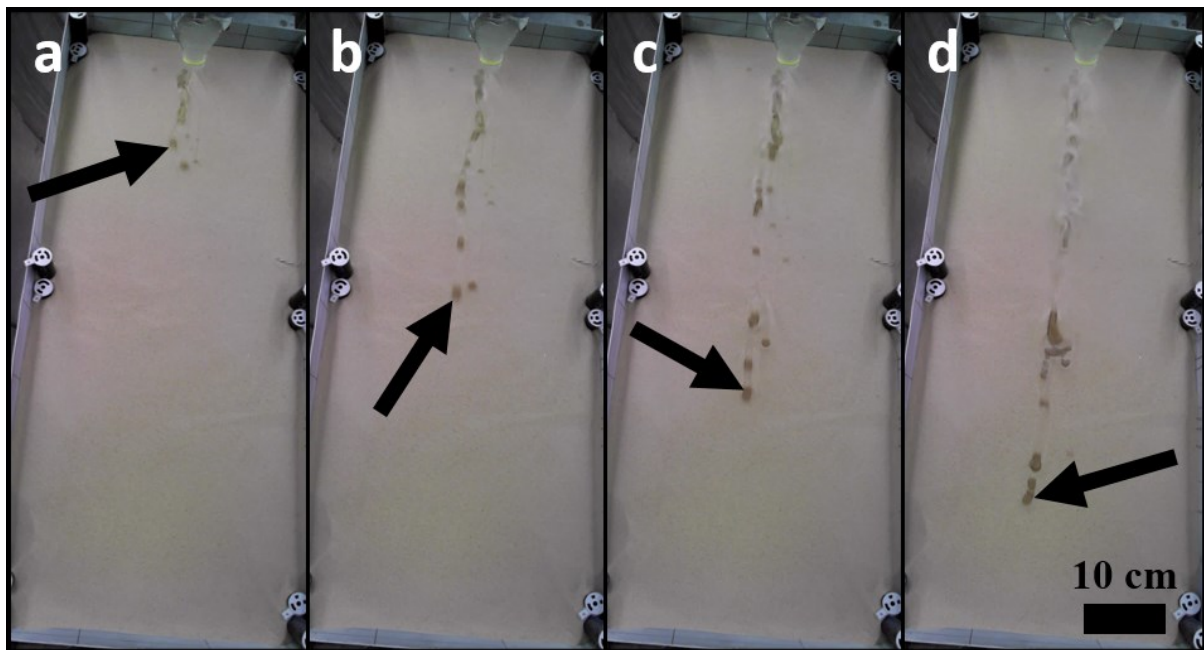


Figure 6: tracking of a pellet undergoing “levitation” (black arrow). The pellet travels around 50 cm in approximately 1 s. Images are taken from the webcam recording of experiment 01.

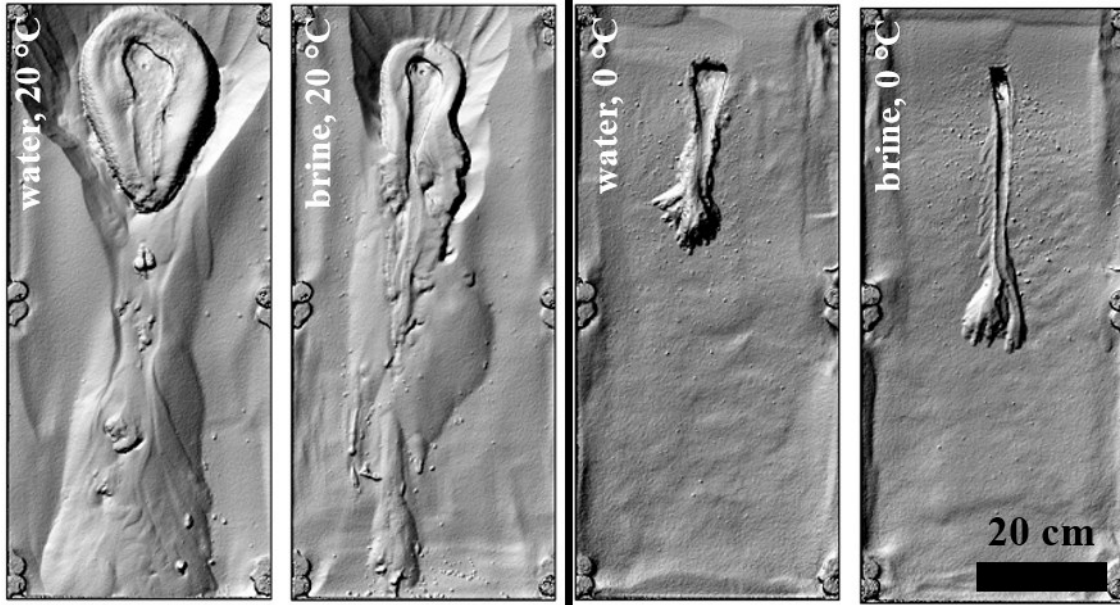


Figure 7: comparison between water and brine flows, at 20 °C and 0 °C. The hillshades displayed here are from experiments 03 (water, 20 °C), 06 (brine, 20 °C), 23 (water, 0 °C) and 20 (brine, 0 °C).

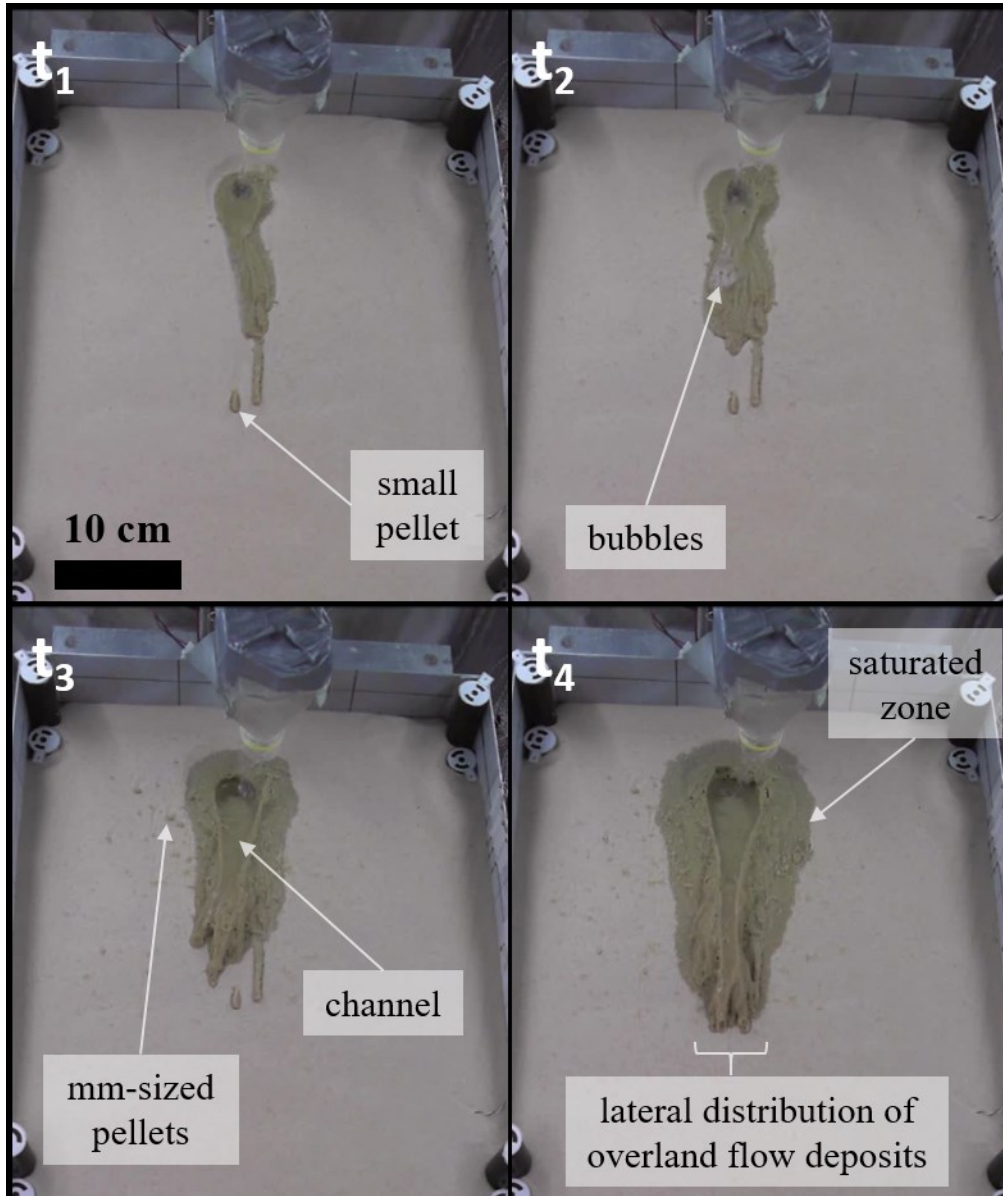


Figure 8: images from experiment 16 (water, 5 °C) at  $t_1 = 5$  s,  $t_2 = 10$  s,  $t_3 = 30$  s,  $t_4 = 60$  s after the beginning of the experiment. We observe the growth of the channel and its deposits, enlargement of the saturated zone and ejection of mm-sized pellets.

### 3.2. Quantification of transport

Our morphological analysis allowed us to quantify the volumes of sediment moved by the different processes described above. The relative volumes moved by these processes differ between hot and cold sediment (Figure 9), we will therefore present the results of these two types of experiments separately.

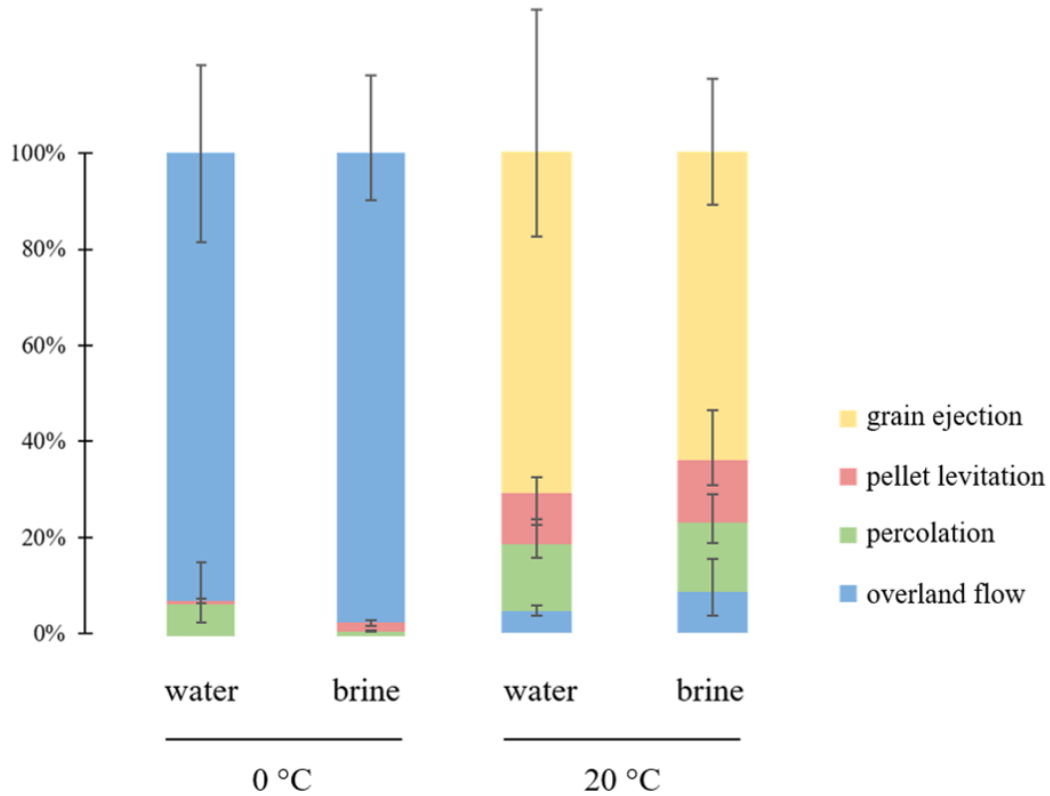


Figure 9: relative contribution of the different processes in the total transported sediment for experiments at 20 °C (left) and 0 °C (right). The relative contributions are averages of all the experiments in each combination of liquid-sand temperature. The error bars show the minimum and maximum values observed in each given combination.

### 3.2.1. Hot experiments

On sediment  $\geq 10$  °C grain ejection induced by boiling is the main sediment transport process because it represents about 55-60 % of the total transported volume (Figure 9). The fine deposits formed by boiling (unit 5) represent only small amounts of sediment that are very difficult to discern on orthoimages or hillshades, and are therefore negligible. We also observed that intense boiling lasts longer for water than for brines at these temperatures: from ~15 s longer at 20 °C to ~25 s longer at 15 °C (Figure 10).

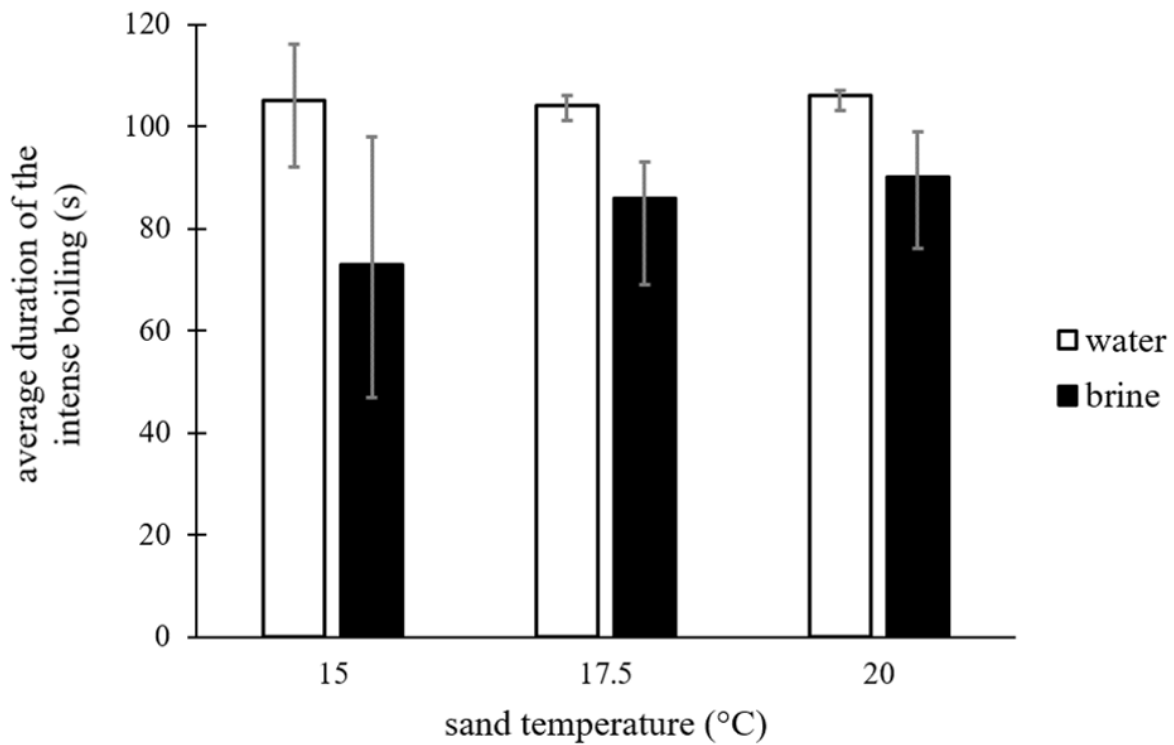


Figure 10: average duration of the intense boiling for water and brine at 15, 17.5 and 20 °C. The error bars are defined as the shortest and the longest boiling durations observed at the different sand temperatures.

Experiments with water also show larger volumes transported through grain ejection caused by boiling (depression/avalanche deposits) than experiments with brine, and larger total volumes transported (Figure 11). Water transports 1.6 times more sediments than brine at 20 °C and 1.5 times more at 17.5 °C. The mean transported volumes at 15 °C are however similar. The volumes of depression/avalanche deposits and the total volume transported increase with temperature (Figure 11).

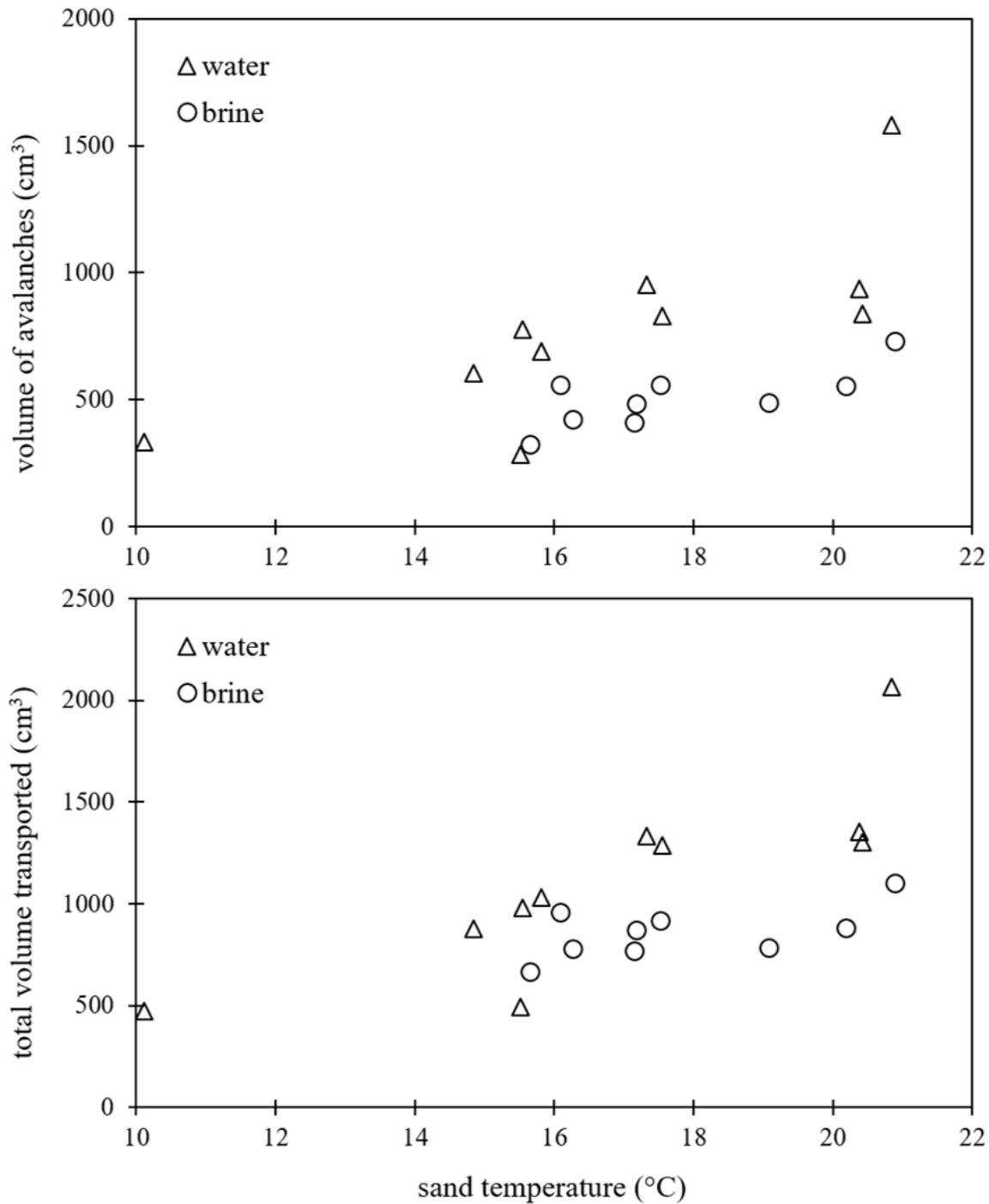


Figure 11: volume transported through avalanche deposits (top) and total volume transported (bottom) in water (triangles) and brine experiments (circles) vs. sand temperature. The experiments displayed here are the “hot” ones (temperatures from 10 °C to 20 °C). The errors are presented in [Table 1](#) and fall within the symbols.

### 3.2.2. Cold experiments

At sand temperatures of 0-5 °C sediment transport is mainly driven by overland flow ([Figure 9](#)). The volumes transported are negligible compared with the hot experiments (< 100 cm<sup>3</sup>), and no difference can be seen between water and brine flows ([Figure 12](#)). Volumes of sediment transported during the cold experiments also seem to be steady against sand temperature, unlike the volumes transported during hot experiments ([Figure 12](#)).

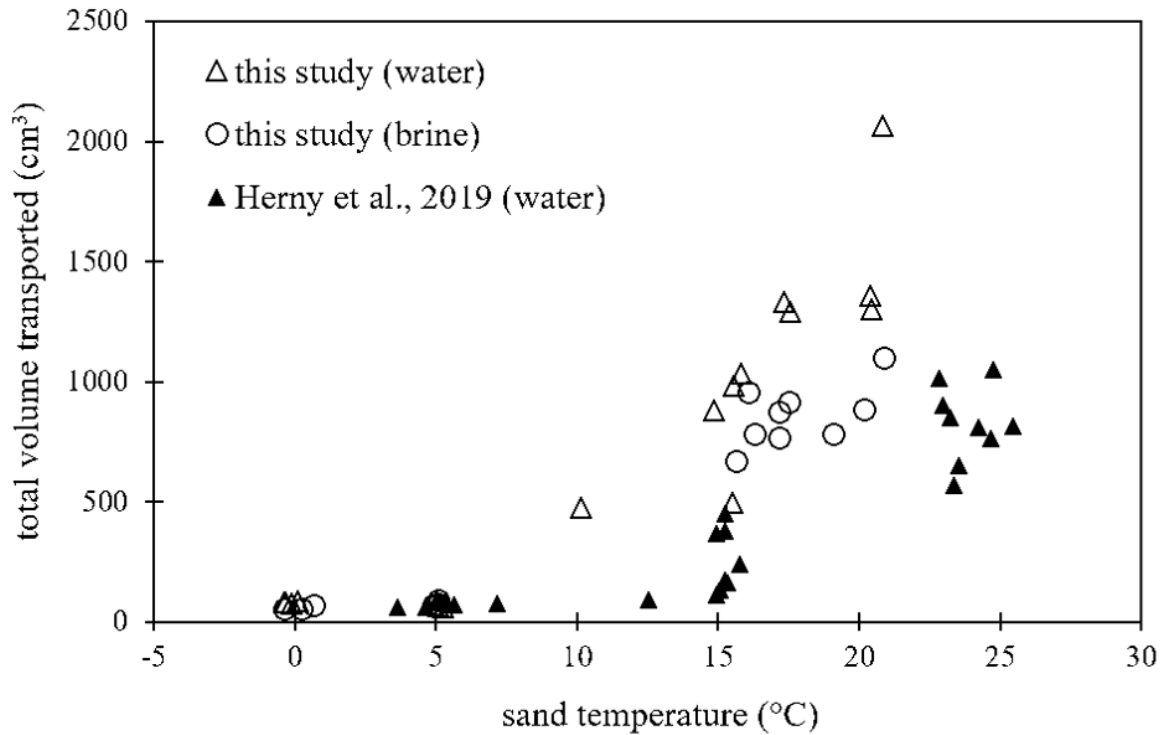


Figure 12: total volume of sediment moved vs. sand temperature in our experiments (water = hollow triangles, brine = hollow circles), and in the experiments of Herny et al. (2019) (filled triangles), which were exclusively experiments with water. The errors are presented in [Table 1](#) and fall within the symbols.

### 3.3. Morphological differences

Channels formed by brine overland flows are longer and narrower than those formed by water overland flows ([Figure 13](#)). This difference is even more visible in cold experiments because the main feature forming at those temperatures is the channel ([Figure 7](#)). Moreover, both water and brine channels tend to be shorter and wider with increasing temperature ([Figure 13](#)). Brine flows tend to produce larger volumes of pellets than water flows ([Figure 14](#)), which most of the time leads to more chaotic morphologies ([Figure 15](#)). We observed a jump in the volume of pellets transported for our three hottest experiments ([Figure 14](#)). Our values of volume of pellets transported by water flows are in agreement with the ones measured by Herny et al. (2019). They also observed a jump in the volume of pellets transported for some of their experiments ([Figure 14](#)), despite not counting buried pellets.

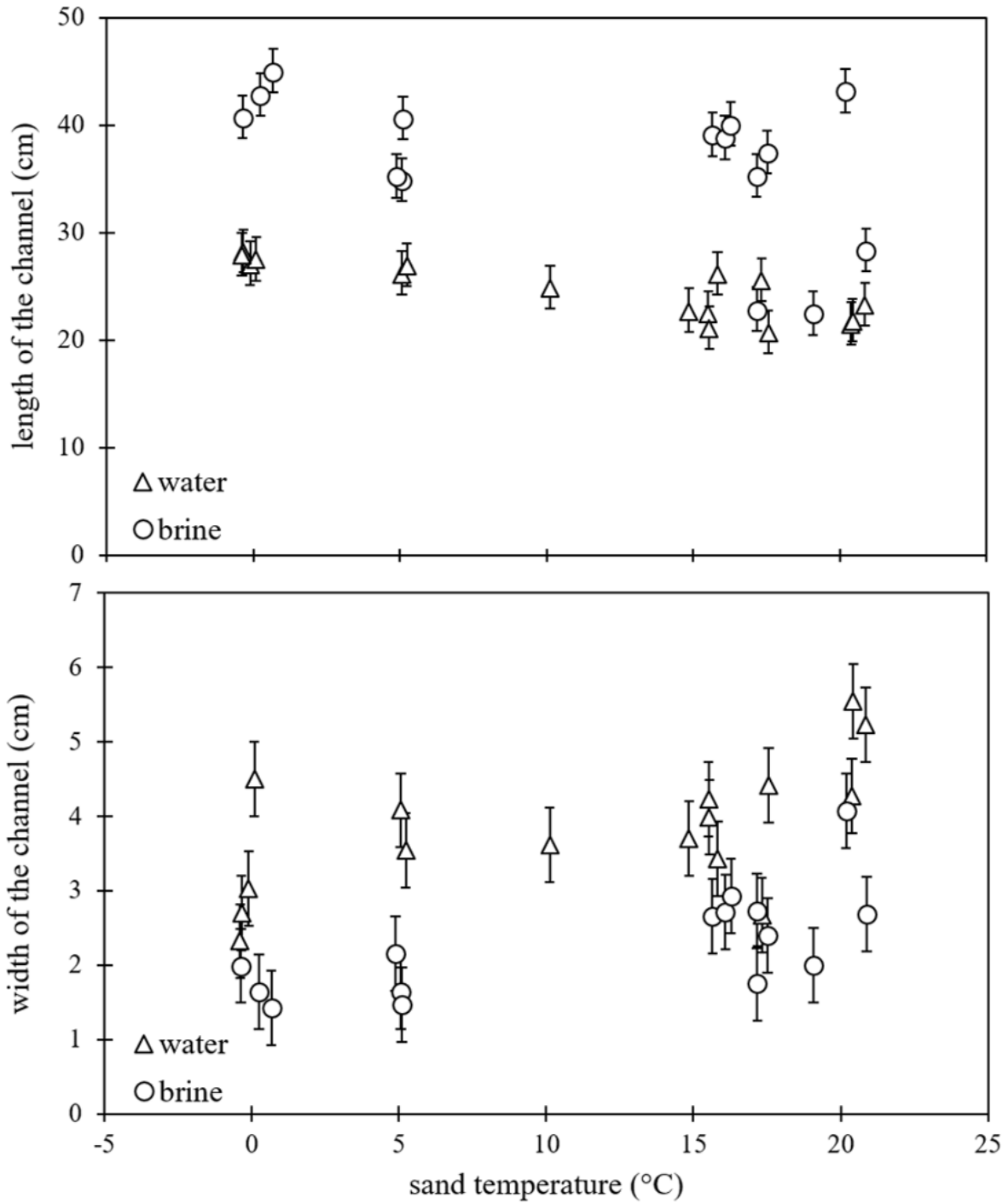


Figure 13: length (top) and width (bottom) of the channel vs. sand temperature, for water (triangles) and brine experiments (circles). The errors in the sand temperature fall within the symbols. The errors in the length and width of the channels have been estimated at respectively 2 cm and 0.5 cm

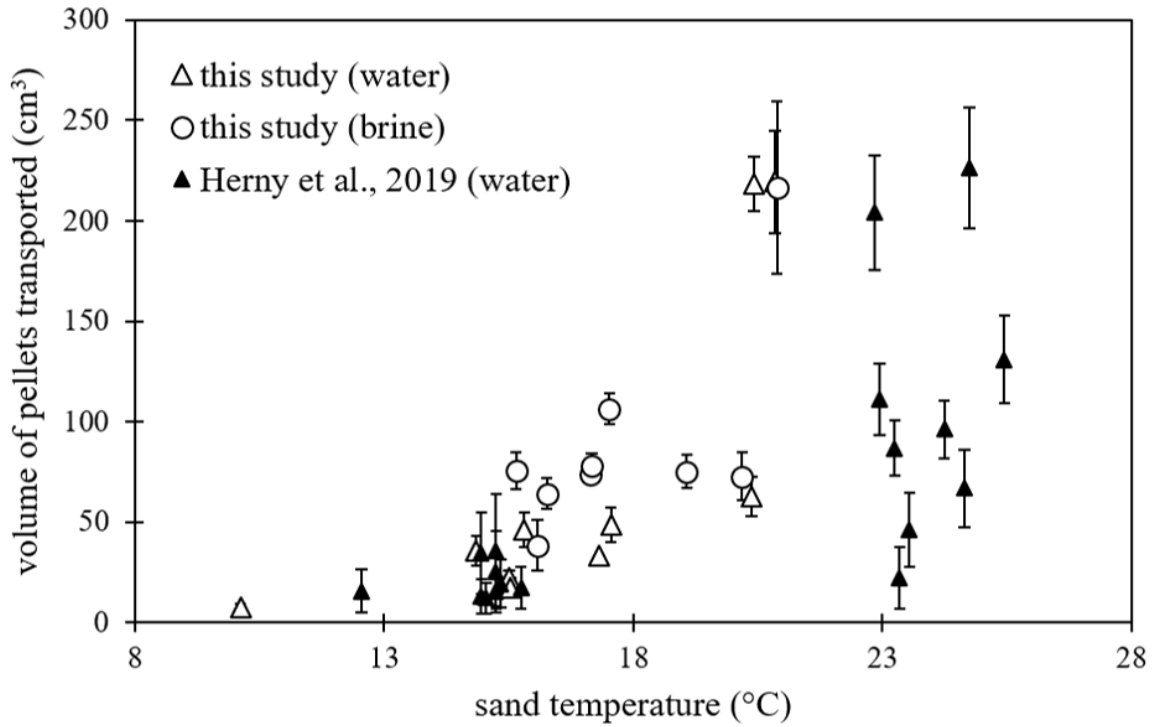


Figure 14: volume of pellets moved vs. sand temperature. The experiments displayed here are the “hot” ones (sand temperature from 10 °C to 20 °C). The data from Herny et al. (2019) are added as small black triangles, and are water flows experiments only. The volume of covered pellets (our unit 6) was not measured by Herny et al. (2019). The error bars on the sand temperature are negligible.

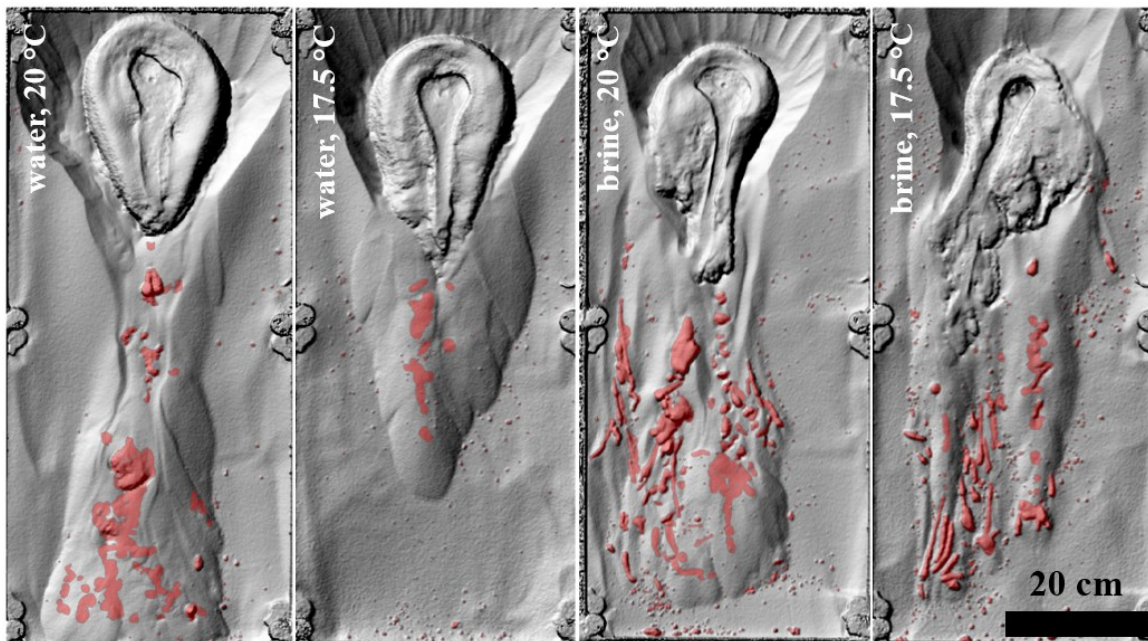


Figure 15: comparison between water and brine flows, at 20 °C and 17.5 °C. Pellets are identified with the light red colour. A lot more pellets are formed with the brine flows and the resulting morphologies seem more chaotic. The hillshades displayed here are from experiments 03 (water, 20 °C), 05 (brine, 20 °C), 25 (water, 17.5 °C) and 30 (brine, 17.5 °C).

## 4. Discussion

In the following section, we will first detail the similarities we observed between our experimental water and brine releases. We will then discuss qualitatively and quantitatively on how sediment is transported during our experiments, and how it links to the physical parameters we measure. We then attempt to scale up our experiments to Mars, based on calculations made in the literature of similar experiments ([Section 2.3.](#)). Finally, we compare our physical parameter measurements to the Martian surface conditions, either measured from orbit or computed with a one-dimensional climate model.

### 4.1. Similarity water/brine

We observed slightly larger volumes of sediment transported by water flows in contrast to brine flows ([Figure 11](#)). This result can be explained by the instability of water under our experimental conditions, which leads to a longer duration of boiling of water flows ([Figure 10](#)). Moreover, our brine solution has a higher density than pure water (1.21 compared with 1 g/cm<sup>3</sup>), so for the same weight of liquid used, brine releases were 1.21 times less voluminous. Hence, water releases form larger volumes of avalanche deposits formed by grain ejection ([Figure 11](#)) - which is the main sediment transport process at those temperatures ([Figure 9](#)), leading to greater total volumes of sediment moved. We found similar ratios of volume of sediment transported/volume of liquid release between water and brine flows (see [Section 4.2](#)).

To summarize, differences between water and brine flows in terms of transported volumes are small on hot sediment (10 °C – 20 °C). On cold sediment (0 °C – 5 °C) the difference is even smaller ([Figure 12](#)).

### 4.2. Sediment transport & comparison with previous studies

Water and brine flows have similar behaviours under Martian pressure, despite slightly larger volumes of sediment transported by water flows (see [Section 4.1](#)) – a behaviour already noted by Massé et al. (2016). Because they used the same protocol, we can combine our results with the ones obtained by Herny et al. (2019) ([Figure 12](#)). The results from Raack et al. (2017) are not displayed here as they come from the same experiments as Herny et al. (2019). Also, compared with Raack et al. (2017) and Herny et al. (2019), we extended the temperature range at which the experiments were conducted.

Total volumes transported during the cold experiments (0 °C – 5 °C) seem to be steady against sand temperature, but experiments on hot sand (10 °C – 20 °C) appear to transport more sediment with increasing temperature ([Figure 12](#)) – in accordance with Herny et al. (2019). On a cold substrate, fluid parameters such as viscosity or flow speed drive the capacity to erode and carry sediments, which is expressed by the different morphologies of channels ([Figure 13](#); [Section 3.3](#)). On hot sediment the volume transported by a liquid release (water or brine) mostly is due to boiling ([Figure 11](#); [Section 3.1.2](#)); it therefore strongly depends on the intensity and duration of boiling, which is driven by the physical parameters: temperature, atmospheric pressure and  $p[\text{H}_2\text{O}]$ . At 7 mbar and 0 °C, water is around the triple point, where the three states of water coexist. When its temperature increases, for example when in contact with the sand in our experiments, the temperature increases above the liquidus on the phase diagram of water. The further temperature is from its liquidus, the more intensely water will boil, and therefore larger volumes of sediment are transported during the hot experiments. Adding salt to pure water, as we did, induces changes in the phase diagram, which are “freezing-point depression” and “boiling-point elevation”. A brine solution, therefore, boils at a higher temperature. It means that at the same temperature (15-20 °C in our case), the temperature is further from the liquidus of water than the liquidus of a brine, and thus pure water boils more intensely. Note that the intensity of boiling, and thus the volume of avalanche deposits and the total volume of sediment moved, depends more specifically on  $p[\text{H}_2\text{O}]$  – and not exactly on the sand temperature. However the boiling occurs within the sand, and we cannot access the relative humidity of the sand bed from our setup – which is necessary to calculate  $p[\text{H}_2\text{O}]$ .

We observe that the trend that emerges from the data of Herny et al. (2019) is similar to the one that emerges from our data: very small amounts of sediment are transported on cold sand (which seem to be independent of the sand temperature); then a jump in transported volumes occurs, after which

transported volumes increase proportionally to the increase in sand temperature. The position of the jump is correlated to the onset of intense boiling. However, the data of Herny et al. (2019) show systematically lower volumes moved ([Figure 12](#)). This difference can be explained by the fact that the vacuum pump we used during our experiments was able to maintain more stable pressures than the one used by Raack et al. (2017) and Herny et al. (2019). Relative humidity and pressure in the MSC tend to increase before decreasing at the beginning of each experiment which causes negative feedback in the boiling process. If this effect is limited, then the atmosphere of the MSC remains more favourable to intense boiling, and therefore to larger volumes of sediment transported by grain ejection. This outcome is consistent with the peaks of pressure observed: during our experiments at 15 °C it rose to 8.6 mbar on average, compared with 11.4 mbar during the experiments of Herny et al. (2019). It also seems that the jump observed by Herny et al. (2019) happens at a higher temperature than ours: their experiments at 15 °C show a range of volumes moved which is between the volumes moved by their 5 °C-experiments and their 25 °C-ones ([Figure 12](#)). In our study, the volumes transported during the experiments at 15 °C are much larger than the volumes transported during the “cold” ones; moreover, we also observed intense boiling during our only experiment at 10 °C ([Figure 12](#)). This result suggests that if the pressure and relative humidity increase is limited at the beginning of the experiment, the boiling is more intense and it can be active at colder surface temperatures. Because this increase would be nearly null on the surface of Mars, this would mean that boiling could be more efficient in transporting sediment and would be triggered at colder temperatures than those observed during our experiments.

We also find that boiling is a very efficient way to transport sediment under Martian conditions: our water releases can transport from 1.6 (at 15 °C) to 3.3 times (at 20 °C) their volumes in sediment. Brine experiments show ratios of the same order of magnitude: 2.0 (at 15 °C) to 2.6 times (at 20 °C) their volume in sediment. Hence, boiling is at least ten times more efficient than overland flows in transporting sediment (ratio volume of sediment transported/volume of liquid release  $\approx$  0.1 - 0.2).

#### *4.3. Scaling up to Mars*

In the following Section, our attempt to scale our experiments up to Mars is based on scaling calculations made for similar experiments, in Massé et al. (2016) and Raack et al. (2017). In their calculations, they take into consideration the effect of the reduced Martian gravity on the physical processes they observed or measured during their experiments. We summarise their methodology in [Section 2.3](#).

Massé et al. (2016) scaled the grain transport by boiling to reduced Martian gravity and concluded that it would be around three times more efficient in terms of volumes of sediment transported, and would lead to morphologies  $\sim$  2.5 times bigger. Using our previous calculations on the ratio volume of sediment moved/volume of water, it means that water or brine flows on a 20 °C sediment could transport from  $\sim$  four to eight times the volume of water in sediment. Our experiments on 20 °C sediment showed that water can transport sediment far from the release source (in 2/3 of the experiments avalanche deposits progress was blocked by the tray). Assuming a reasonable length of around one metre for our experiments, the same process on Mars would form morphologies of several metres in length which would be visible at least on images from the High Resolution Imaging Science Experiment (HiRISE) at 25 cm/pixel. Based on our previous calculations, brine flows containing an equivalent amount of water should transport similar volumes of sediment. It is however worth noticing that brine releases produce more pellets than water releases ([Figure 14](#)). Considering that pellet “levitation” is thought to last much longer under the reduced Martian gravity ( $\sim$  48 times longer; Raack et al., 2017), and that brine flows are more likely to occur than pure water flows, brine releases on Mars could result in morphologies much longer than those we calculated (potentially of an order of magnitude), with similar amounts of water. It allows us to confirm and extend the conclusion of Raack et al. (2017), that the boiling phenomenon could create morphologies with much less water or brine than has been estimated previously (Chojnacki et al., 2016; Grimm et al., 2014; Malin and Edgett, 2000; Stillman et al., 2016). However, scaling morphologies to Mars is challenging, and many more parameters should be taken into account to describe the potential boiling of a Martian aqueous flow (e.g. the flow rate, temperature variations, potential slow temperature increase, a potential cyclicality). The simple-scaling arguments made above demonstrate that the boiling phenomenon should be explored to resolve the issue of the high water budget thought to form some aqueous mass movement features on Mars.

#### 4.4. Comparison with Mars surface conditions

Our experiments show that intense boiling is triggered at a sand temperature between 5 °C and 15 °C (Figure 12). Because a non-intense boiling (i.e. bubbling) is observed during 0 °C-experiments and 5 °C-experiments and as the only experiment at 10 °C also shows intense boiling (Figure 12), we think it could even be triggered between 5 °C and 10 °C. Also, both water and brine have been observed to remain liquid when flowing on 0 °C-sand and 5 °C-sand (water starts forming ice features at 0 °C but remains mostly liquid).

We applied a 1D version of the LMD Mars climate model physics (Forget et al., 1999; Spiga and Forget, 2008) to the Martian slopes, in a similar way to Conway et al. (2018). This model takes into account several parameters: latitude, slope angle and orientation, the thermal inertia of the substrate, orbital obliquity and solar longitude of perihelion (LsP; solar longitude at which the planet is the closest from the Sun) as variables; surface pressure and soil albedo were fixed, respectively 6.1 mbar and 0.2 (Conway et al., 2018). We compute from the model results the number of hours per year when the surface conditions allow to reach or exceed a certain temperature (Figure 16). This model shows that positive surface temperatures are common on Mars at the present day (current obliquity = 25°; current LsP = 251°; standard Mars thermal inertia  $\approx 250 \text{ Jm}^{-2}\text{K}^{-1}\text{s}^{-1/2}$ , Putzig et al., 2005). Slopes at large ranges of latitudes and angles experience surface temperatures exceeding 0 °C for more than 1000 h/yr (> 40 sols), and temperatures above 5 °C are not uncommon either (nearly all equator-facing slopes with an angle  $\geq 20^\circ$ ). Temperatures of 15 °C are more difficult to reach, but still possible (Figure 16). Trends can be identified (Figure 16): i. on equator-facing slopes, temperatures are more often positive and go higher than on pole-facing ones; ii. equator-facing slopes with greater angles also reach more recurrent and higher positive temperatures; the reverse is observable on pole-facing slopes; iii. positive temperatures are more common at mid-latitudes. All these trends stem from the orbital parameters of Mars. Here the southern hemisphere undergoes more positive-temperature periods than the northern hemisphere due to the closeness of its summer solstice with the current LsP of Mars.

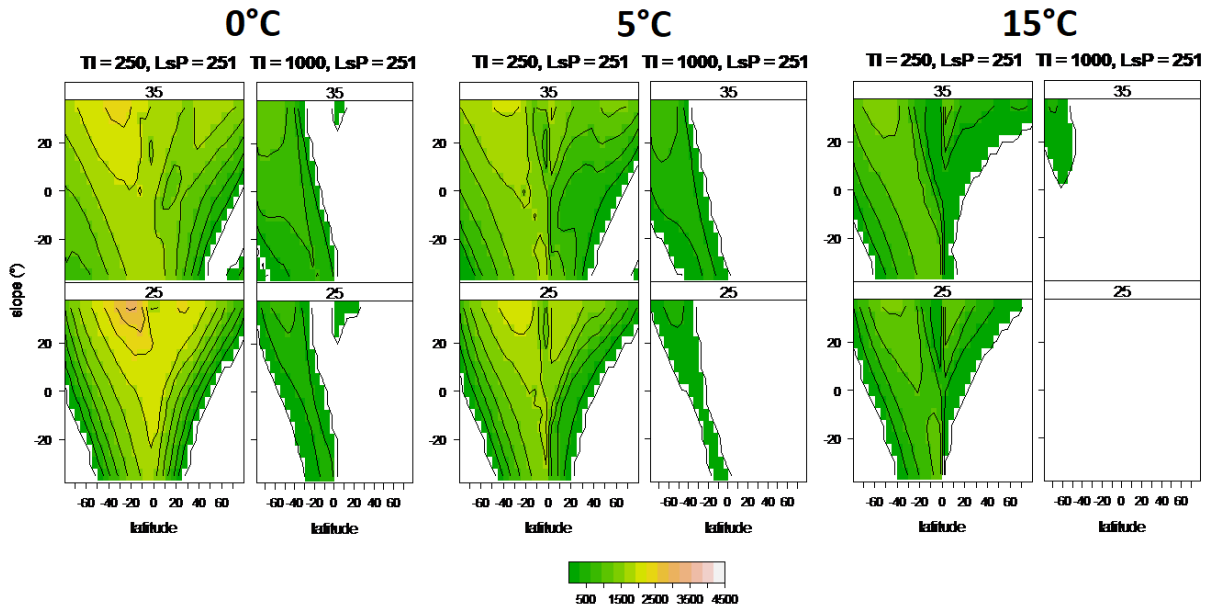


Figure 16: slope angle vs. latitude, with the number of hours per year (h/yr) when the surface temperature exceeds 0 °C (left columns), 5 °C (middle columns) and 15 °C (right columns) given in the colour scale. Positive slope angles indicate equator-facing slopes, negative slope angles indicate pole-facing ones. For each surface temperature, columns have thermal inertia of  $250 \text{ Jm}^{-2}\text{K}^{-1}\text{s}^{-1/2}$  (left column) and  $1000 \text{ Jm}^{-2}\text{K}^{-1}\text{s}^{-1/2}$  (right column), values we chose to represent respectively mean Mars and bedrock (Ferguson et al., 2006; Putzig et al., 2005). On the top line are the calculations with an orbital obliquity of 35°, representing Mars' recent past; on the bottom line are calculations with an obliquity of 25° (current value). The LsP here is fixed at its current value (251°).

Moreover, McEwen et al., (2011, 2014) and Ojha et al. (2014) reported from orbital thermal data surface temperatures exceeding  $\sim 15$  °C to over 25 °C during summer, in the southern mid-latitudes and in some places at equatorial latitudes (e.g. Valles Marineris).

Linking our experimental data with surface temperature measurements and modelling, we can determine that liquid water and brine flow should boil on Mars' surface at the present day given a water source. Surface temperatures required to maintain and boil a water flow would be reached quite easily; brine flows could occur at even lower temperatures than 0 °C because of their freezing point depression, and therefore are even more likely to occur (Brass, 1980). Moreover, Rivera-Valentín et al. (2020) concluded that, thanks to metastability, brines could be found at even more locations than previously thought (Davila et al., 2010); for instance, the  $\text{Ca}(\text{ClO}_4)_2$  brine is thought to be stable or metastable for  $\sim 2$  % of the Martian year, on  $\sim 40$  % of the Martian surface. Moreover, previous studies confirmed that brines tend to persist beyond their predicted stability region, as metastable aqueous (Fischer et al., 2016) or supercooled solutions (Toner et al., 2014). Therefore, liquid brines have the potential to be found nearly everywhere on the surface of Mars.

Also, in the past few million years positive surface temperatures were even more widespread, as well as overall higher than today because of higher orbital obliquity (Figure 16; Kreslavsky et al., 2008). Such temperatures should have led to metastable and boiling water (or more likely brines) for a higher number of sols per year compared with the present day. Therefore, their boiling could have triggered the formation of mass-wasting features in the mid-latitudes to high-latitudes.

Overall, these observations show that it has been, and still is, possible to reach surface conditions on Mars where water and brine can flow and boil. The questions remain, however, whether (1) these phenomena occur (or occurred) and led to mass-wasting features, and (2) today we can observe those features – active or as remnants of past activity. The potential source of water is still unknown and has been debated in several studies (e.g., Abotalib and Heggy, 2019; Grimm et al., 2014; Stillman et al., 2014, 2016).

## 5. Conclusions

Several conclusions emerge from our study:

1. During our experiments, we observed similar flow behaviours compared with Raack et al. (2017) and Herny et al. (2019) – indicating good reproducibility of those experiments. In “cold” experiments ( $\leq 5$  °C), sediment transport mainly is driven by overland flows. In “hot” experiments, above a certain threshold in temperature (between 5 °C and 10 °C), boiling is triggered and becomes the process transporting the largest volumes of sediment. It can transport over three times the weight of water in sediment, which is  $\sim$  ten times more efficient than overland flows.
2. Water and brine flows produce similar volumes of sediment moved, but they present morphological differences: brine flows tend to produce more levitating pellets, which produce longer morphologies than grain ejection by boiling.
3. Scaled to Mars, the morphologies formed by grain ejection would be several metres long. Moreover, pellet “levitation” should occur for longer under Martian conditions: morphologies resulting from brine releases could thus be an order of magnitude longer than those resulting from water releases, for a similar amount of water. In both cases, metre or tens-of-metre-long features would be visible on HiRISE imagery.
4. Comparing our experimental results to a 1D-climatic model and direct surface temperature measurements, we find that it is possible to reach atmospheric conditions favourable to water stability and boiling on present-day Mars. In particular, a wide range of slopes undergo over 40 sols per year of positive temperatures. Atmospheric conditions favourable to brine stability and boiling are even more widespread thanks to the depression of their freezing point. Moreover, within the last million years, periods of higher obliquity have led to higher temperatures overall, suggesting that water and brine stability and boiling could have been sporadically even more widespread during the recent past.

## Acknowledgements

We thank the reviewer Paul Carling and the editors Alessandro Morbidelli and Elizabeth Rampe for constructive comments that greatly improved the quality of the manuscript. The laboratory work was supported by the Europlanet 2020 RI which has received funding from the European Union's Horizon 2020 research and innovation program under grant agreement No 654208, by Région Pays de la Loire project GeoPlaNet (convention N° 2016-10982) and by the French Space Agency (CNES). SRL thanks the UK Space Agency for support under grants ST/R001405/1, ST/W002949/1 and ST/S00145X/1. CM is funded by the Agence Nationale de la Recherche in the framework of the project ANR-19-CE01-0010 PERMOLARDS. MRP acknowledges funding from the UK Space Agency under grants ST/V005332/1 and ST/V002295/1.

## Competing interests

Authors declare no competing interest.

## Data availability

Part of the datasets related to this article (DoDs, units outline, raw data table, videos of experiments) can be found at <https://doi.org/10.6084/m9.figshare.20375880.v7>, hosted at figshare. Contact authors for specific queries concerning datasets not hosted here.

## References

- Abotalib, A.Z., Heggy, E., 2019. A deep groundwater origin for recurring slope lineae on Mars. *Nature Geoscience* 12, 235–241. <https://doi.org/10.1038/s41561-019-0327-5>
- Bolles, R.C., Baker, H.H., Marimont, D.H., 1987. Epipolar-plane image analysis: An approach to determining structure from motion. *Int J Comput Vision* 1, 7–55. <https://doi.org/10.1007/BF00128525>
- Brass, G.W., 1980. Stability of brines on Mars. *Icarus* 42, 20–28. [https://doi.org/10.1016/0019-1035\(80\)90237-7](https://doi.org/10.1016/0019-1035(80)90237-7)
- Chojnacki, M., McEwen, A., Dundas, C., Ojha, L., Urso, A., Sutton, S., 2016. Geologic context of recurring slope lineae in Melas and Coprates Chasmata, Mars: GEOLOGY OF MELAS AND COPRATES RSL. *J. Geophys. Res. Planets* 121, 1204–1231. <https://doi.org/10.1002/2015JE004991>
- Clark, B.C., Kounaves, S.P., 2016. Evidence for the distribution of perchlorates on Mars. *International Journal of Astrobiology* 15, 311–318. <https://doi.org/10.1017/S1473550415000385>
- Conway, S.J., Harrison, T.N., Lewis, S.R., 2018. Martian Gullies and Their Connection With the Martian Climate, in: *Dynamic Mars*. Elsevier, pp. 87–119. <https://doi.org/10.1016/B978-0-12-813018-6.00003-0>
- Conway, S.J., Lamb, M.P., Balme, M.R., Towner, M.C., Murray, J.B., 2011. Enhanced runout and erosion by overland flow at low pressure and sub-freezing conditions: Experiments and application to Mars. *Icarus* 211, 443–457. <https://doi.org/10.1016/j.icarus.2010.08.026>
- Davila, A.F., Duport, L.G., Melchiorri, R., Jänchen, J., Valea, S., de los Rios, A., Fairén, A.G., Möhlmann, D., McKay, C.P., Ascaso, C., Wierzchos, J., 2010. Hygroscopic Salts and the Potential for Life on Mars. *Astrobiology* 10, 617–628. <https://doi.org/10.1089/ast.2009.0421>
- Dickson, J.L., Head, J.W., Kreslavsky, M., 2007. Martian gullies in the southern mid-latitudes of Mars: Evidence for climate-controlled formation of young fluvial features based upon local and global topography. *Icarus* 188, 315–323. <https://doi.org/10.1016/j.icarus.2006.11.020>
- Farley, K.A., Williford, K.H., Stack, K.M., Bhartia, R., Chen, A., de la Torre, M., Hand, K., Goreva, Y., Herd, C.D.K., Hueso, R., Liu, Y., Maki, J.N., Martinez, G., Moeller, R.C., Nelessen, A., Newman, C.E., Nunes, D., Ponce, A., Spanovich, N., Willis, P.A., Beegle, L.W., Bell, J.F., Brown, A.J., Hamran, S.-E., Hurowitz, J.A., Maurice, S., Paige, D.A., Rodriguez-Manfredi, J.A., Schulte, M., Wiens, R.C., 2020. Mars 2020 Mission Overview. *Space Sci Rev* 216, 142. <https://doi.org/10.1007/s11214-020-00762-y>

- Fergason, R.L., Christensen, P.R., Kieffer, H.H., 2006. High-resolution thermal inertia derived from the Thermal Emission Imaging System (THEMIS): Thermal model and applications: THEMIS THERMAL INERTIA. *J. Geophys. Res.* 111, n/a-n/a. <https://doi.org/10.1029/2006JE002735>
- Fischer, E., Martínez, G.M., Rennó, N.O., 2016. Formation and Persistence of Brine on Mars: Experimental Simulations throughout the Diurnal Cycle at the Phoenix Landing Site. *Astrobiology* 16, 937–948. <https://doi.org/10.1089/ast.2016.1525>
- Forget, F., Hourdin, F., Fournier, R., Hourdin, C., Talagrand, O., Collins, M., Lewis, S.R., Read, P.L., Huot, J.-P., 1999. Improved general circulation models of the Martian atmosphere from the surface to above 80 km. *J. Geophys. Res.* 104, 24155–24175. <https://doi.org/10.1029/1999JE001025>
- Gasda, P.J., Haldeman, E.B., Wiens, R.C., Rapin, W., Bristow, T.F., Bridges, J.C., Schwenzer, S.P., Clark, B., Herkenhoff, K., Frydenvang, J., Lanza, N.L., Maurice, S., Clegg, S., Delapp, D.M., Sanford, V.L., Bodine, M.R., McInroy, R., 2017. In situ detection of boron by ChemCam on Mars: First Detection of Boron on Mars. *Geophys. Res. Lett.* 44, 8739–8748. <https://doi.org/10.1002/2017GL074480>
- Gendrin, A., 2005. Sulfates in Martian Layered Terrains: The OMEGA/Mars Express View. *Science* 307, 1587–1591. <https://doi.org/10.1126/science.1109087>
- Graf, J., Zurek, R., Jones, R., Eisen, H., Johnston, M.D., Jai, B., Mateer, B., 2002. An overview of the Mars Reconnaissance Orbiter mission, in: *Proceedings, IEEE Aerospace Conference*. Presented at the 2002 IEEE Aerospace Conference, IEEE, Big Sky, MT, USA, pp. 1–180. <https://doi.org/10.1109/AERO.2002.1036837>
- Grimm, R.E., Harrison, K.P., Stillman, D.E., 2014. Water budgets of martian recurring slope lineae. *Icarus* 233, 316–327. <https://doi.org/10.1016/j.icarus.2013.11.013>
- Grotzinger, J.P., Crisp, J., Vasavada, A.R., Anderson, R.C., Baker, C.J., Barry, R., Blake, D.F., Conrad, P., Edgett, K.S., Ferdowski, B., Gellert, R., Gilbert, J.B., Golombek, M., Gómez-Elvira, J., Hassler, D.M., Jandura, L., Litvak, M., Mahaffy, P., Maki, J., Meyer, M., Malin, M.C., Mitrofanov, I., Simmonds, J.J., Vaniman, D., Welch, R.V., Wiens, R.C., 2012. Mars Science Laboratory Mission and Science Investigation. *Space Sci Rev* 170, 5–56. <https://doi.org/10.1007/s11214-012-9892-2>
- Haberle, R.M., McKay, C.P., Schaeffer, J., Cabrol, N.A., Grin, E.A., Zent, A.P., Quinn, R., 2001. On the possibility of liquid water on present-day Mars. *J. Geophys. Res.* 106, 23317–23326. <https://doi.org/10.1029/2000JE001360>
- Hecht, M.H., Kounaves, S.P., Quinn, R.C., West, S.J., Young, S.M.M., Ming, D.W., Catling, D.C., Clark, B.C., Boynton, W.V., Hoffman, J., DeFlores, L.P., Gospodinova, K., Kapit, J., Smith, P.H., 2009. Detection of Perchlorate and the Soluble Chemistry of Martian Soil at the Phoenix Lander Site. *Science* 325, 64–67. <https://doi.org/10.1126/science.1172466>
- Heldmann, J.L., Mellon, M.T., 2004. Observations of martian gullies and constraints on potential formation mechanisms. *Icarus* 168, 285–304. <https://doi.org/10.1016/j.icarus.2003.11.024>
- Herny, C., Conway, S.J., Raack, J., Carpy, S., Colleu-Banse, T., Patel, M.R., 2019. Downslope sediment transport by boiling liquid water under Mars-like conditions: experiments and potential implications for Martian gullies. *Geological Society, London, Special Publications* 467, 373–410. <https://doi.org/10.1144/SP467.10>
- Kreslavsky, M.A., Head, J.W., Marchant, D.R., 2008. Periods of active permafrost layer formation during the geological history of Mars: Implications for circum-polar and mid-latitude surface processes. *Planetary and Space Science* 56, 289–302. <https://doi.org/10.1016/j.pss.2006.02.010>
- Malin, M.C., Edgett, K.S., 2000. Evidence for Recent Groundwater Seepage and Surface Runoff on Mars. *Science* 288, 2330–2335. <https://doi.org/10.1126/science.288.5475.2330>
- Massé, M., Conway, S.J., Gargani, J., Patel, M.R., Pasquon, K., McEwen, A., Carpy, S., Chevrier, V., Balme, M.R., Ojha, L., Vincendon, M., Poulet, F., Costard, F., Jouannic, G., 2016. Transport processes induced by metastable boiling water under Martian surface conditions. *Nature Geosci* 9, 425–428. <https://doi.org/10.1038/ngeo2706>
- McEwen, A.S., Dundas, C.M., Mattson, S.S., Toigo, A.D., Ojha, L., Wray, J.J., Chojnacki, M., Byrne, S., Murchie, S.L., Thomas, N., 2014. Recurring slope lineae in equatorial regions of Mars. *Nature Geosci* 7, 53–58. <https://doi.org/10.1038/ngeo2014>

- McEwen, A.S., Ojha, L., Dundas, C.M., Mattson, S.S., Byrne, S., Wray, J.J., Cull, S.C., Murchie, S.L., Thomas, N., Gulick, V.C., 2011. Seasonal Flows on Warm Martian Slopes. *Science* 333, 740–743. <https://doi.org/10.1126/science.1204816>
- Morino, C., Conway, S.J., Balme, M.R., Helgason, J.K., Sæmundsson, Þ., Jordan, C., Hillier, J., Argles, T., 2021. The impact of ground-ice thaw on landslide geomorphology and dynamics: two case studies in northern Iceland. *Landslides* 18, 2785–2812. <https://doi.org/10.1007/s10346-021-01661-1>
- Morino, C., Conway, S.J., Balme, M.R., Hillier, J., Jordan, C., Saemundsson, Þ., Argles, T., 2019. Debris-flow release processes investigated through the analysis of multi-temporal LiDAR datasets in north-western Iceland: Debris-flow processes investigated by multi-temporal LiDAR datasets. *Earth Surf. Process. Landforms* 44, 144–159. <https://doi.org/10.1002/esp.4488>
- Ojha, L., McEwen, A., Dundas, C., Byrne, S., Mattson, S., Wray, J., Masse, M., Schaefer, E., 2014. HiRISE observations of Recurring Slope Lineae (RSL) during southern summer on Mars. *Icarus* 231, 365–376. <https://doi.org/10.1016/j.icarus.2013.12.021>
- Putzig, N.E., Mellon, M.T., Kretke, K.A., Arvidson, R.E., 2005. Global thermal inertia and surface properties of Mars from the MGS mapping mission. *Icarus* 173, 325–341. <https://doi.org/10.1016/j.icarus.2004.08.017>
- Raack, J., Conway, S.J., Herny, C., Balme, M.R., Carpy, S., Patel, M.R., 2017. Water induced sediment levitation enhances downslope transport on Mars. *Nat Commun* 8, 1151. <https://doi.org/10.1038/s41467-017-01213-z>
- Rivera-Hernández, F., Sumner, D.Y., Mangold, N., Stack, K.M., Forni, O., Newsom, H., Williams, A., Nachon, M., L'Haridon, J., Gasnault, O., Wiens, R., Maurice, S., 2019. Using ChemCam LIBS data to constrain grain size in rocks on Mars: Proof of concept and application to rocks at Yellowknife Bay and Pahrump Hills, Gale crater. *Icarus* 321, 82–98. <https://doi.org/10.1016/j.icarus.2018.10.023>
- Rivera-Valentín, E.G., Chevrier, V.F., Soto, A., Martínez, G., 2020. Distribution and habitability of (meta)stable brines on present-day Mars. *Nat Astron* 4, 756–761. <https://doi.org/10.1038/s41550-020-1080-9>
- Schmidt, R., 2003. Mars Express—ESA's first mission to planet Mars. *Acta Astronautica* 52, 197–202. [https://doi.org/10.1016/S0094-5765\(02\)00157-1](https://doi.org/10.1016/S0094-5765(02)00157-1)
- Schorghofer, N., Aharonson, O., Khatiwala, S., 2002. Slope streaks on Mars: Correlations with surface properties and the potential role of water: SLOPE STREAKS ON MARS. *Geophys. Res. Lett.* 29, 41-1-41–4. <https://doi.org/10.1029/2002GL015889>
- Spiga, A., Forget, F., 2008. Fast and accurate estimation of solar irradiance on Martian slopes. *Geophys. Res. Lett.* 35, L15201. <https://doi.org/10.1029/2008GL034956>
- Squyres, S.W., Grotzinger, J.P., Arvidson, R.E., Bell, J.F., Calvin, W., Christensen, P.R., Clark, B.C., Crisp, J.A., Farrand, W.H., Herkenhoff, K.E., Johnson, J.R., Klingelhöfer, G., Knoll, A.H., McLennan, S.M., McSween, H.Y., Morris, R.V., Rice, J.W., Rieder, R., Soderblom, L.A., 2004. In Situ Evidence for an Ancient Aqueous Environment at Meridiani Planum, Mars. *Science* 306, 1709–1714. <https://doi.org/10.1126/science.1104559>
- Stillman, D.E., Michaels, T.I., Grimm, R.E., Hanley, J., 2016. Observations and modeling of northern mid-latitude recurring slope lineae (RSL) suggest recharge by a present-day martian briny aquifer. *Icarus* 265, 125–138. <https://doi.org/10.1016/j.icarus.2015.10.007>
- Stillman, D.E., Michaels, T.I., Grimm, R.E., Harrison, K.P., 2014. New observations of martian southern mid-latitude recurring slope lineae (RSL) imply formation by freshwater subsurface flows. *Icarus* 233, 328–341. <https://doi.org/10.1016/j.icarus.2014.01.017>
- Sylvest, M.E., Conway, S.J., Patel, M.R., Dixon, J.C., Barnes, A., 2016. Mass wasting triggered by seasonal CO<sub>2</sub> sublimation under Martian atmospheric conditions: Laboratory experiments. *Geophys. Res. Lett.* 43. <https://doi.org/10.1002/2016GL071022>
- Sylvest, M.E., Dixon, J.C., Conway, S.J., Patel, M.R., McElwaine, J.N., Hagermann, A., Barnes, A., 2019. CO<sub>2</sub> sublimation in Martian gullies: laboratory experiments at varied slope angle and regolith grain sizes. *Geological Society, London, Special Publications* 467, 343–371. <https://doi.org/10.1144/SP467.11>

- Thomas, N.H., Ehlmann, B.L., Meslin, P. -Y., Rapin, W., Anderson, D.E., Rivera-Hernández, F., Forni, O., Schröder, S., Cousin, A., Mangold, N., Gellert, R., Gasnault, O., Wiens, R.C., 2019. Mars Science Laboratory Observations of Chloride Salts in Gale Crater, Mars. *Geophys. Res. Lett.* 46, 10754–10763. <https://doi.org/10.1029/2019GL082764>
- Toner, J.D., Catling, D.C., Light, B., 2014. The formation of supercooled brines, viscous liquids, and low-temperature perchlorate glasses in aqueous solutions relevant to Mars. *Icarus* 233, 36–47. <https://doi.org/10.1016/j.icarus.2014.01.018>
- Weitz, C.M., Sullivan, R.J., Lapotre, M.G.A., Rowland, S.K., Grant, J.A., Baker, M., Yingst, R.A., 2018. Sand Grain Sizes and Shapes in Eolian Bedforms at Gale Crater, Mars. *Geophys. Res. Lett.* 45, 9471–9479. <https://doi.org/10.1029/2018GL078972>
- Westoby, M.J., Brasington, J., Glasser, N.F., Hambrey, M.J., Reynolds, J.M., 2012. ‘Structure-from-Motion’ photogrammetry: A low-cost, effective tool for geoscience applications. *Geomorphology* 179, 300–314. <https://doi.org/10.1016/j.geomorph.2012.08.021>
- [Williams, R.D., 2012. DEMs of Difference. \*Geomorphological Techniques\*.](#)
- Zelenyi, L.M., Korablev, O.I., Rodionov, D.S., Novikov, B.S., Marchenkov, K.I., Andreev, O.N., Larionov, E.V., 2015. Scientific objectives of the scientific equipment of the landing platform of the ExoMars-2018 mission. *Sol Syst Res* 49, 509–517. <https://doi.org/10.1134/S0038094615070229>